https://doi.org/10.5194/egusphere-2026-2840
Preprint. Discussion started: 16 June 2026


# Speleothem sulphate and trace elements constrain Alpine glacial inception across the Marine Isotope Stage 11/10 transition

Jonathan L. Baker[1], Alexandre Honiat[1], Peter M. Wynn[2], Jens Fohlmeister[3], Martin Trüssel[4], Samuel Hollowood[5], Jiaoyang Ruan[6,7], Regina Mertz-Kraus[8], R. Lawrence Edwards[9], and Christoph Spötl[1]

1. Institute of Geology, Universität Innsbruck, Innrain 52f, 6020 Innsbruck, Austria
2. Lancaster Environment Centre, Lancaster University, Lancaster LA1 4YQ, United Kingdom
3. German Federal Office for Radiation Protection (BfS), Berlin, Germany
4. Foundation Naturerbe Karst und Höhlen Obwalden (NeKO), Alpnach, Switzerland
5. Department of Earth Sciences, University of Oxford, Wellington Square, Oxford OX1 2JD, United Kingdom
6. IBS Center for Climate Physics, Institute for Basic Science, Busan, South Korea
7. State Key Laboratory of Lithospheric and Environmental Coevolution, Institute of Geology and Geophysics, Chinese Academy of Sciences, Beijing, China
8. Institute for Geosciences, Johannes Gutenberg Universität Mainz, Saarstraße 21, 55122 Mainz, Germany
9. Department of Earth Sciences, University of Minnesota, 116 Church St SE, Minneapolis, MN 55455, USA

*Correspondence to:* jonathan.baker@uibk.ac.at

Keywords: subglacial, speleothem paleoclimatology, mountain glacier, sulphide oxidation, stable isotope, sulphur

https://doi.org/10.5194/egusphere-2026-2840
Preprint. Discussion started: 16 June 2026


**Abstract**

Alpine glacier histories beyond the Last Glacial Maximum are poorly resolved, impeding our ability to test how mountain glaciers respond to dynamic forcings on orbital to sub-orbital timescales. This gap may be addressed through proxy records from alpine caves, in which subglacial speleothem growth is facilitated by recharge beneath temperate glaciers through sulphide-bearing epikarst. However, the use of conventional stable isotopes of carbon ($\delta^{13}C$) and oxygen ($\delta^{18}O$) in speleothem calcite yields ambiguities when interpreting environmental transitions and ice cover during glacial inception and retreat. Herein, we present a multiproxy speleothem record from Betten Cave (Melchsee Frutt, central Swiss Alps) spanning 415–360 ka that integrates sulphate stable isotopes ($\delta^{34}S_{SO4}$, $\delta^{18}O_{SO4}$) and trace-element geochemistry with calcite $\delta^{13}C$–$\delta^{18}O$ to diagnose redox state, sulphide-oxidation pathways, and hydrological reorganization across the Marine Isotope Stage 11/10 glacial inception. Three environmental phases are identified from this dataset, marking the transition from (1) a vegetated and soil-covered montane valley to (2) a soil-limited periglacial setting, hydrologically influenced by glacier advance through the adjacent valley (~2,000 m a.s.l.), to (3) subglacial speleothem growth, in which a temperature glacier covered the lowest elevation of the cave system (~1,700 m a.s.l.). After 402 ± 4 ka, a long-term decrease in the isotopic offset between water and aqueous sulphate ($\Delta\delta^{18}O_{SO4–H2O}$) records progressive oxygen limitation concomitant with glacier thickening and advance over the cave site by 372 ± 3 ka. Coeval peaks in cations and redox-sensitive transition metals reflect the enhanced delivery of glacially comminuted detritus and coupled Fe–Mn redox cycling within the subglacial karst system. These results directly link sulphate oxygen- and sulphur-isotope systematics and trace-element fingerprints to glacier dynamics, providing geochronologically precise benchmarks and a transferable framework for reconstructing mountain glacier behaviour where geomorphic records are incomplete.

## 1. Main Text

### *1.1 Introduction*

Major glaciations and deglaciations have shaped the landscape of the European Alps at least since the Mid-Pleistocene transition (Preusser et al., 2021; Reitner, 2022), due to the amplification of Earth system responses to orbital forcings from feedbacks such as greenhouse forcing, thermohaline circulation, and expansion of the polar cryosphere (Bajo et al., 2020; Seguinot et al., 2018). However, most of these mountain glacier advances are known mostly from outwash deposits in the alpine foreland and associated ice-marginal deposits and landforms (Fiebig and Preusser, 2008; Ivy-Ochs et al., 2022b; Monegato et al., 2023; Preusser, 2004). Within montane regions, only deposits and landforms linked to the last deglaciation as well as Late Glacial to Holocene re-advances are documented (e.g., Ivy-Ochs et al., 2022a; Schimmelpfennig et al., 2014), and to a limited extent those of the Last Glacial Maximum from ~32–22 ka and the

https://doi.org/10.5194/egusphere-2026-2840
Preprint. Discussion started: 16 June 2026


subsequent deglaciation (Ivy-Ochs et al., 2022a). Despite intensive study, the glacier history of many individual catchments remains poorly constrained, largely due to preservation biases that promote the erosion of surficial deposits and limited chronological precision in periglacial foreland sediments. The Melchsee Frutt region of central Switzerland (~2000 m a.s.l.) is one such valley (Fig. 1), and while it preserves clear geomorphic evidence of Pleistocene glacial erosion in the form of steep ridges, glaciokarst, and depressions filled by lakes, the chronology and extent of ice advances and retreats prior to the Last Glacial Maximum (LGM) are largely unknown. Filling this knowledge gap is crucial in the attempt to constrain the long-term sensitivity of the alpine cryosphere to dynamic forcings, albeit on geologically abrupt (suborbital to sub-centennial) time scales (Clauzel et al., 2023).

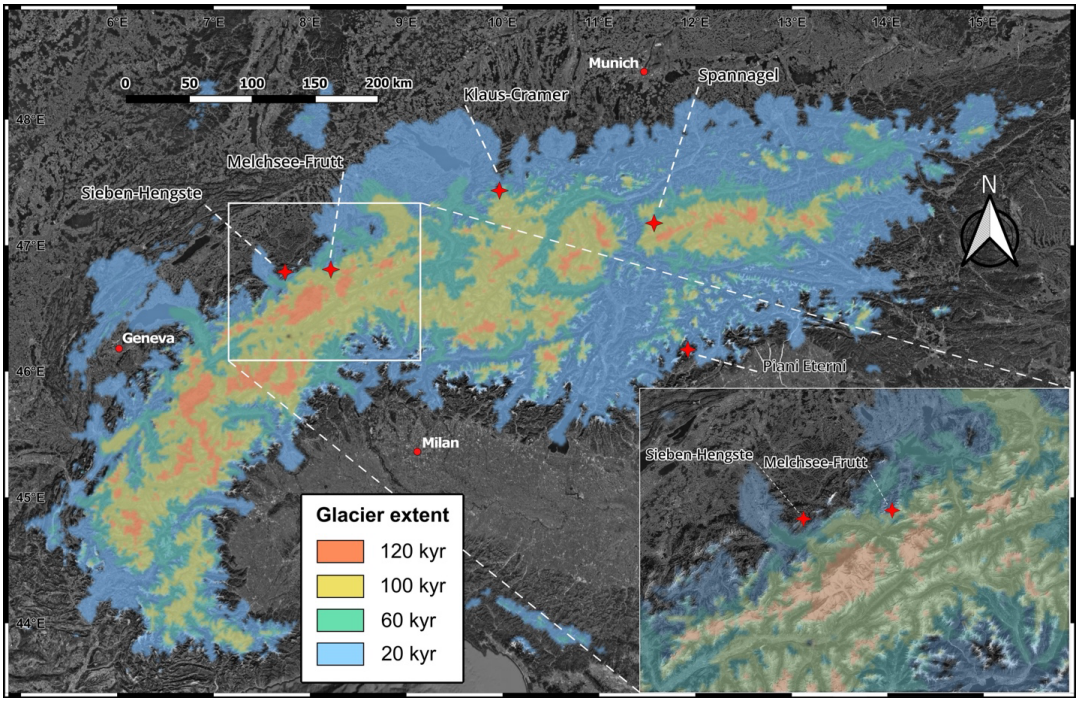


**Figure 1:** Regional geography of the European alps and study area (inset). Red stars denote alpine cave sites potentially located within the ice margin during glacial maxima: Sieben Hengste; Melchsee Frutt (this study); Klaus Cramer; Spannagel; Piani Eterni. Color shading plots the simulated glacier extent at four intervals during the last glacial period, according to the coupled-climate ice model from Jouvet et al. (2023).

Contemporary alpine glaciers and periglacial landscapes in Switzerland are now restricted to elevations above 1800 m a.s.l. (Sommer et al., 2020). They remain critical freshwater resources but are rapidly retreating as a consequence of accumulated anthropogenic warming (Haeberli et

https://doi.org/10.5194/egusphere-2026-2840
Preprint. Discussion started: 16 June 2026


al., 2007; Sommer et al., 2020), whose rate is locally twice that of the Northern Hemisphere (Kotlarski et al., 2023). With a nearly 40% observed loss in glacier mass since 2000 C.E. (Zemp et al., 2025), glaciers in the Alps are poised to still lose half of their current mass within decades (Zekollari et al., 2025). Reconstructing past glacier dynamics in such settings is therefore essential for understanding cryospheric sensitivity to climate dynamics beyond the range of forcings observed within the instrumental and geomorphic records.

### *1.2 Paleoclimate records in alpine karst*

Speleothems from caves in the European Alps provide one of the only semi-continuous archives of mountain environments extending well beyond the last glacial period, with currently published records extending to Marine Isotope Stage (MIS) 11 in the north/central Alps (Boch et al., 2011; Fohlmeister et al., 2023; Honiat et al., 2026; Li et al., 2021; Skiba et al., 2023a; Spötl et al., 2008; Wilcox et al., 2020) and discontinuously to MIS 10 in the southern Alps (Columbu et al., 2018). Measurements of stable carbon and oxygen isotopes in these radiometrically dated samples have been successfully utilized to reconstruct both orbital-scale glacial–interglacial transitions and millennial-scale variability such as Dansgaard–Oeschger cycles (Moseley et al., 2020; Spötl et al., 2006) and Heinrich stadials (Li et al., 2021). In these systems, speleothem $\delta^{18}O$ primarily reflects the isotopic composition of precipitation as a function of regional temperature and synoptic air circulation (Luetscher et al., 2015), whereas $\delta^{13}C$ is commonly interpreted in terms of soil cover and respiration rates (Fohlmeister et al., 2020), modulated by in-cave processes such as prior carbonate precipitation (PCP) (Skiba et al., 2023a; Skiba and Fohlmeister, 2023).

### *1.3 Subglacial speleothems extend glacier reconstructions*

In high-elevation cave settings, $\delta^{13}C$ values below host-rock compositions indicate soil-derived $CO_2$ input, while values equal to or higher than host-rock $\delta^{13}C$ may reflect soil-free conditions, either in barren periglacial landscapes or beneath warm-based glaciers (Columbu et al., 2018; Spötl and Mangini, 2007). In the latter scenario, strongly reduced or absent soil-$CO_2$ production leads to a reduction in the dissolved $CO_2$ of infiltrating water, limiting carbonic-acid dissolution (CAD) of the host rock, which can slow or halt the deposition of speleothems. However, the oxidation of sulphide minerals—whether disseminated in the host rock or surface detritus—leads to the production of sulphuric acid in surface and ground water, commonly in association with glaciated terrains (Fairchild et al., 1999; Graly and Rezvanbehbahani, 2022; Hubbard and Nienow, 1997; Sharp et al., 1999; Zarroca et al., 2021). Sulphuric-acid dissolution (SAD) of carbonate host rock allows speleothem deposition to continue despite the advance of warm-based glaciers over the cave site (Spötl et al., 2024).

https://doi.org/10.5194/egusphere-2026-2840
Preprint. Discussion started: 16 June 2026


Based on available alpine speleothem records from the last glacial period, paired with transient ice modelling of the European Alps (Seguinot et al., 2018), Skiba et al. (2023a) found that speleothem $\delta^{13}C$ is generally a reliable indicator of mountain glaciers, especially if enrichment of $^{13}C$ from PCP can be constrained. Similarly, Spötl et al. (2024) found that when compared to global datasets, most of these subglacial speleothems plot within a distinct bivariate cluster characterized by high $\delta^{13}C$ and low $\delta^{18}O$. However, the use of a $\delta^{13}C$ threshold can only determine when sulphide oxidation is likely to have a dominant effect on dissolution processes. Since natural acid-rock drainage effects have been observed downstream from retreating glaciers (Fortner et al., 2011), and sulphide oxidation can influence $\delta^{13}C$ in non-glaciated alpine cave systems (Bajo et al., 2017; Columbu et al., 2018), precise reconstructions of mountain glaciers from speleothem records require additional proxies to delineate these environments.

Glaciation fundamentally alters weathering rates and regimes through mechanical denudation and the exposure of fine detritus to fresh meltwater (Hawkings et al., 2025; Prestrud Anderson et al., 1997; Stachnik et al., 2016; Torres et al., 2017; Wadham et al., 2010). When sulphide oxidation is prevalent, the elevated concentration of certain trace elements in meltwater reflects the mobilization of metal sulphides and subsequent dissolution of acid-soluble minerals or leaching of clay minerals (Ilyashuk and Ilyashuk, 2024; Stachnik et al., 2016). Reductive dissolution of oxide minerals via $Fe^{3+}$, generated by sulphide-oxidising bacteria in subglacial environments (Sharp et al., 1999), can amplify the redox cycling of trace metals sorbed or co-precipitated by metal (oxyhydr)oxides (Montross et al., 2013; Neal et al., 2001). In principle, these processes can be captured by secondary mineral deposits in caves (Frierdich et al., 2011), but such trace-element geochemistry has not been thoroughly investigated in subglacial speleothems.

The effects of sulphide oxidation on the dissolution regime and aqueous sulphate inventory are expected to be greater in a subglacial setting than non-glaciated alpine karst, due to the large amounts of finely comminuted sediments and thus exposure of fresh mineral surfaces enhancing chemical reactivity (Colombo et al., 2019; Fairchild et al., 1999; Sharp et al., 1999; Williams et al., 2006). Furthermore, during the loss of soil and equilibration of surface $pCO_2$ with the glacial atmosphere, the dominance of SAD leads to an excess of $Ca^{2+}$ and high $[SO_4^{2-}]/[HCO_3^-]$ in karst waters (Graly and Rezvanbehbahani, 2022; Wadham et al., 2010), enhancing the potential for PCP (Skiba et al., 2023a) and causing a nearly complete shift toward host rock-derived carbon in speleothem calcite, with very minor contributions from atmospheric $CO_2$. This alteration to the sulphur cycle should lead to high concentrations of subglacial speleothem sulphate, which ought to be derived principally from the oxidation of sulphides (Wadham et al., 2007). Because sedimentary sulphides are typically strongly depleted in $^{34}S$, enhanced sulphide oxidation produces low $\delta^{34}S$ values in sulphate produced by the reaction (Bottrell, 2007; Samborska et al., 2013; Sun et al., 2017; Taylor and Wheeler, 1993), which is preserved in speleothems (Wynn et al., 2008).

In parallel, $\delta^{18}O$ of sulphate reflects the relative contribution of oxygen from atmospheric $O_2$ versus water, with lower values indicating greater incorporation of water-derived oxygen under oxygen-

https://doi.org/10.5194/egusphere-2026-2840
Preprint. Discussion started: 16 June 2026


limited or low-pH environments (Bottrell and Tranter, 2002; Wadham et al., 2007; Wynn et al., 2006). As glacier hydrological systems and subglacial weathering environments become more frequently disconnected from the surface atmosphere, low redox conditions become a regular feature of ice-covered environments. This transition causes a distinctive change in the chemical composition of meltwaters transiting subglacial environments of low redox status, particularly with regard to the $\delta^{18}O_{SO4}$ signature and the abundance of redox-sensitive elements. Together, these proxies may record the onset of glaciation and track the redox state and hydrological connectivity of the subglacial environment.

A recently established composite stable-isotope record, comprising four overlapping stalagmites from Betten Cave in the Melchsee Frutt region, spans the interval 415–360 ka and documents the climatic transition from MIS 11c to MIS 10 (Honiat et al., 2026). The stepwise increase (decrease) in $\delta^{13}C$ ($\delta^{18}O$) values of calcite is interpreted to demarcate the evolution of the alpine environment from a vegetated plateau (415–402 ka) to a glaciated landscape (402–372 ka), followed by the expansion of a warm-based glacier at 372 ± 3 ka. The MIS 10 glaciation is only identified in a few foreland sequences (Ivy-Ochs et al., 2022b; Preusser et al., 2021), but high chronological uncertainty precludes investigation of the climate dynamics underlying the glacial inception. Herein we build on the interpretation of $\delta^{13}C$ and $\delta^{18}O$ by Honiat et al. (2026) to characterize the evolution of the MIS 11/10 alpine environment using geochemical proxies common to the investigation of sulphide oxidation and weathering in modern karst aquifers and subglacial environments (Bottrell and Tranter, 2002; Colombo et al., 2019; Graly and Rezvanbehbahani, 2022; Taylor and Wheeler, 1993; Wynn et al., 2006). If successful, our dataset would advance the potential of alpine speleothem records to fill gaps in the chronology of Early–Middle Pleistocene glaciations, as well as provide precise benchmarks for the calibration of modelling reconstructions (Jouvet et al., 2023; Seguinot et al., 2018) and forecasts (Cook et al., 2023) of the alpine cryosphere.

## 2. Materials and Methods

### *2.1 Minor cation and trace-element analysis*

Elemental analysis by laser-ablation inductively coupled plasma mass spectrometry (LA-ICP-MS) was performed in line-scan mode at the Institute of Geosciences, JGU Mainz, Germany, using an ESI NWR193 ArF excimer laser ablation system with a TwoVol2 cell (193 nm wavelength), coupled to an Agilent 7700x quadrupole ICP-MS. Surfaces were pre-ablated before each scan to remove surface contamination. Line scans were conducted at 15 µm/s using a rectangular beam (130 × 50 µm; 150 × 50 µm for pre-ablation). The laser operated at 10 Hz with energy ~3.5 J/cm². Background intensities were recorded for 15 s.

https://doi.org/10.5194/egusphere-2026-2840
Preprint. Discussion started: 16 June 2026


Element concentrations were calibrated using synthetic glass NIST SRM 610, and quality control materials (QCMs)—USGS MACS-3, USGS BCR-2G, NIST SRM 612—monitored accuracy and precision. $^{43}Ca$ was used as the internal standard, assuming a Ca concentration of 390,000 µg/g for samples and the corresponding GeoReM values for calibration materials and QCMs. Signals were collected in time-resolved mode and processed with iolite4 software. Anomalous peaks associated with surface defects were removed using a 30-point moving median filter in Matlab, after which elemental data were down-interpolated to match the stable-isotope sampling resolution. Elemental values reported in Table S2 reflect this post-processing.

### *2.2 Extraction and stable-isotope analysis of speleothem sulphate*

Duplicate aliquots of powdered calcite, ranging from 75-200 mg, were drilled at 25 intervals for stable-isotope analysis of extracted sulphate ($\delta^{34}S_{SO4}$ and $\delta^{18}O_{SO4}$; Table S3). Each subsample was digested in 1 ml of 4 M HCl acid, after which 0.2 ml of 1 M $BaCl_2$ solution was added to induce the precipitation of $BaSO_4$. Low-sulphate samples were seeded by the addition of either quartz powder (for S) or carbon black (for O) to enhance yield recovery. Precipitation was allowed to proceed during at least 24 hours storage in a refrigerator at <5°C. Solutions were centrifuged for 20 minutes at 3500 rpm, followed by removal of the supernatant and re-suspension in deionized water to remove acidity and chloride content. This step was repeated until the solution pH was >6. Precipitates were dried in a drying cabinet for 24 hours and then stored in a desiccator.

Stable-isotope measurements of S and O were performed by continuous-flow isotope ratio mass spectrometry (Isoprime 100 CF-IRMS) coupled to an elemental analyser (Elementar Pyrocube) at the Lancaster Environment Centre, Lancaster University, UK. Sulphur isotopes were determined by combustion within tin capsules at 1120˚C in the presence of vanadium pentoxide. Oxygen isotopes were analysed by pyrolysis in silver capsules at 1450˚C in the presence of a carbon black catalyst. Values of $\delta^{34}S_{SO4}$ were corrected against VCDT using international standards SO6, SO5 and NBS-127 (assuming $\delta^{34}S$ values of -34.1‰, +0.5‰ and +21.1‰ respectively) and values of $\delta^{18}O_{SO4}$ were corrected against VSMOW using international standards SO6, NBS-127 and IAEA-601 (assuming values of -11.35‰, +9.3‰ and +23.14‰ respectively). Reported 2-σ uncertainties were constrained by repeat measurements of an in-house standard, achieving <0.2 ‰ across all run sequences.

Each subsample yielded sufficient $BaSO_4$ (250–400 µg) for a stable signal and calibration to internal standards, with 1-σ uncertainties better than 0.2‰ for all runs. These yields are consistent with high sulphur concentrations of 1150 ± 470 µg/g $CaCO_3$ (n = 6, 750–1850 µg/g $CaCO_3$), measured by ion chromatography during screening of stalagmite 13, as well as by LA-ICP-MS (Table S2).

https://doi.org/10.5194/egusphere-2026-2840
Preprint. Discussion started: 16 June 2026


### *2.3 Climate model simulations and site-level extraction*

We used the transient Community Earth System Model version 1.2 (CESM1.2) simulation, described in (Timmermann et al., 2022) and (Yun et al., 2023), to provide synoptic-scale climatic context for the speleothem record. The fully coupled atmosphere–ocean–land–sea ice model was run at ~3.8° horizontal resolution with monthly output and forced by time-varying orbital parameters, greenhouse gas concentrations and prescribed ice-sheet boundary conditions consistent with late Middle Pleistocene climate evolution. Differences in 500 hPa geopotential height and 850 hPa wind vectors were estimated by subtracting the means of three intervals represented in Figure S7.

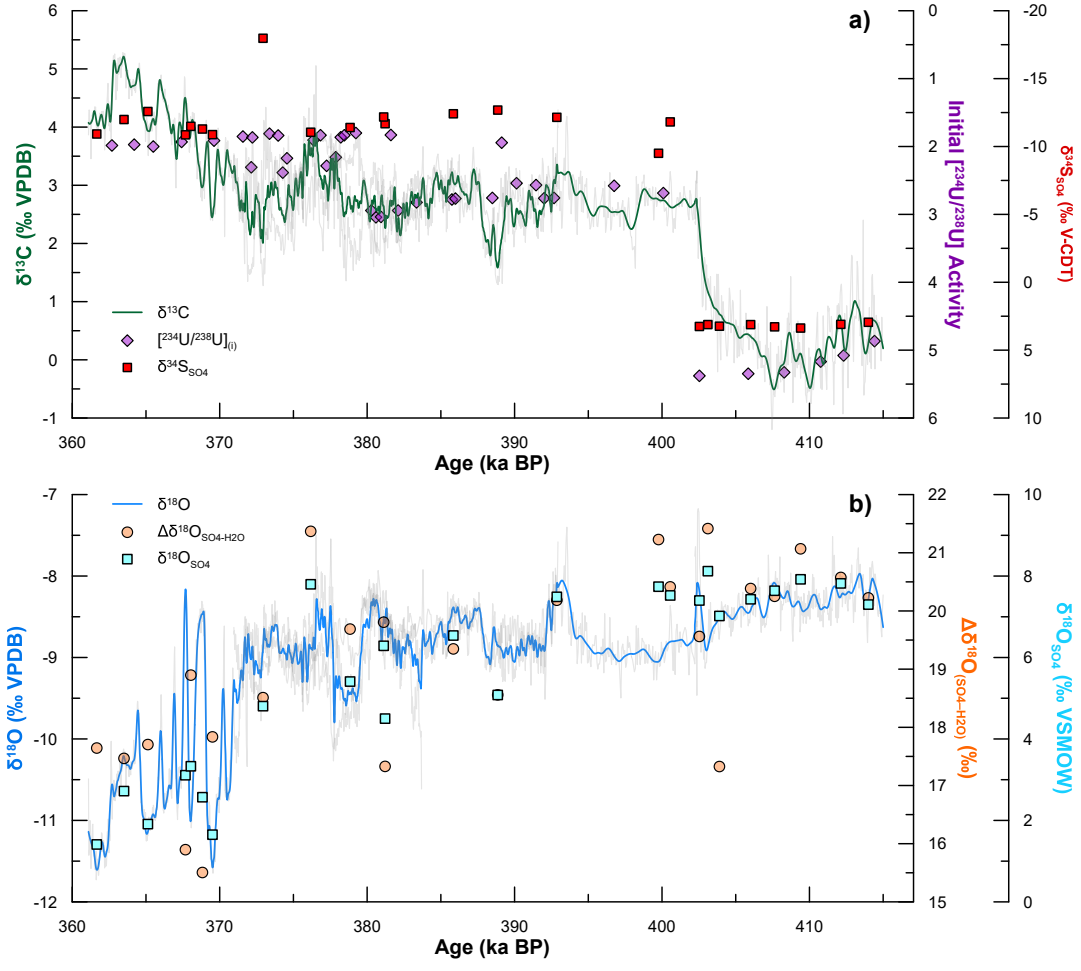


**Figure 2:** Main proxy data results from the Melchsee Frutt speleothem stack. a) Bold green line shows $\delta^{13}C$ after a LOESS smoothing of combined data from all four stalagmites. Light grey lines show original $\delta^{13}C$ of individual

https://doi.org/10.5194/egusphere-2026-2840
Preprint. Discussion started: 16 June 2026


stalagmites (Honiat et al., 2026). Sulphur-isotope composition of speleothem sulphate ($\delta^{34}S_{SO4}$) is denoted by red squares. Initial $^{234}U/^{238}U$ activity ratio (purple diamonds) is calculated from measured value, assuming decay since the U-Th radiometric age. b) Bold blue line shows carbonate $\delta^{18}O$ after a LOESS smoothing of combined data from all four stalagmites. Light grey lines show original $\delta^{18}O$ of individual stalagmites (Honiat et al., 2026). Oxygen-isotope composition of speleothem sulphate ($\delta^{18}O_{SO4}$) is denoted by light blue squares, whereas the isotopic offset between speleothem sulphate and water ($\Delta\delta^{18}O_{(SO4–H2O)}$) is denoted by orange circles.

## 3. Results

### *3.1 Age model and stable isotopes ($\delta^{13}C$ and $\delta^{18}O$) of speleothem calcite*

A total of 42 U–Th analyses were performed across the four stalagmites reported by Honiat et al. (2026) from Betten Cave (designated as 60, 15D, 13, and 61D from youngest to oldest; Fig. S2), yielding well-constrained chronologies. Some variability in sample chemistry and growth conditions may be expected from the fact that each stalagmite was taken from a different part of the cave (Fig. S1a).

Stable-isotope records are largely reproducible between intervals of synchronous growth (Honiat et al., 2026), allowing for the construction of a continuous composite record spanning 415 to 360 ka (Fig. 2). The $\delta^{18}O$ time series is characterized by two main phases. Between 415 and 380 ka, $\delta^{18}O$ values show relatively low variability (~2‰), ranging from approximately −9.5‰ to −7.5‰ (VPDB), with a slight decreasing trend through time. From 380 to 360 ka, there is a distinct increase in variance, with $\delta^{18}O$ values ranging from approximately −11.6‰ to −7.6‰ and exhibiting abrupt fluctuations of up to ~3‰ superimposed on the decreasing trend. The $\delta^{13}C$ record shows more structured variability and can be subdivided into four intervals. From 415 to 408 ka, $\delta^{13}C$ values are relatively stable near 0‰, after which $\delta^{13}C$ increases to +3‰ by 402 ka. From 402 to 372 ka, $\delta^{13}C$ is comparatively stable, whilst in the final interval (372 to 360 ka), $\delta^{13}C$ rises steadily to +5‰.

### *3.2 Stable sulphur and oxygen isotopes of speleothem sulphate*

Values of $\delta^{34}S_{SO4}$ range from -18.0‰ to +3.4‰ (VCDT), but these data cluster tightly into two groups: +3.2 ± 0.1‰ in samples from 415–402 ka; and -11.9 ± 1.7‰ in samples younger than 402 ka. The large negative shift in $\delta^{34}S_{SO4}$ coincides with the termination of the first positive shift in $\delta^{13}C$ values of calcite from 408–402 ka. Values of $\delta^{18}O_{SO4}$ range from +1.4‰ to +8.1‰ (VSMOW), with an arithmetic mean of 5.6 ± 2.3‰ (1 σ). The highest values occur early in the composite record and remain stable near +7–8‰ until the breakpoint at ca. 400 ka. Subsequently, $\delta^{18}O_{SO4}$ follows a significant negative trend ($r$ = -0.68; n = 16) toward the lowest values (+1.4 to 3.3‰) between ca. 360–370 ka. Although this trend is mimicked in calcite $\delta^{18}O$, the magnitude is nearly double in $\delta^{18}O_{SO4}$, causing calcite and sulphate values to converge over time. Conversion of $\delta^{18}O_{CaCO3}$ data to dripwater-equivalent values allowed for an approximation of the oxygen-

https://doi.org/10.5194/egusphere-2026-2840
Preprint. Discussion started: 16 June 2026


isotope offset between water and dissolved aqueous sulphate within the karst system. The resulting offset, termed $\Delta\delta^{18}O_{SO4\text{-}H2O}$, ranged from 15.5‰ to 21.4‰ and exhibited a steady decrease from late MIS 11 (~390 ka) to MIS 10 (Fig. 2b).

### *3.3 Constraints from proxy system modelling in CaveCalc*

We simulated the evolution of speleothem $\delta^{13}C$ and Mg as a function of soil $pCO_2$, dissolution pathways (CAD vs. SAD), prior carbonate precipitation (PCP), and bedrock chemistry (Sect. 3.4) using CaveCalc software (Owen et al., 2018). For growth during MIS 11c, the measured range in $\delta^{13}C$ can be explained at higher $pCO_2$ if SAD exceeds 20% and at least 10% of $Ca^{2+}$ is precipitated prior to the stalagmite (Fig. S3). The higher $\delta^{13}C$ values from 402–360 ka (+3‰ to +6‰) require low $pCO_2$ and SAD above ~70%. These high contributions from SAD generate an excess of $Ca^{2+}$ but impose a molar limit on $[HCO_3^-]$, leading to strong $^{13}C$ enrichment from minimal PCP. Despite initially high $[Ca^{2+}]$ from SAD under these conditions (Fig. S3a), PCP terminates when the fraction of $[Ca^{2+}]$ remaining at the stalagmite apex (*f*Ca) remains above 0.8. Using the Mg/Ca and Sr/Ca values measured in host rock samples (see Sect. 3.4) and the known range in partition coefficients at low temperature, CaveCalc is unable to replicate the observed concentration of speleothem Mg and Sr via enrichment from PCP. However, strong incongruent calcite dissolution (ICD) of the marl interbeds can explain the range of Mg/Ca and Sr/Ca (Fig. S3e-f).

### *3.4 Minor cations and trace elements in speleothems and host rock*

Minor cations of Mg, Sr, and Ba exhibit positive covariance within individual stalagmites, but the relationship is stronger in the younger samples (15D and 60). Slopes of ln(Mg/Ca) vs. ln(Sr/Ca) and ln(Sr/Ca) vs. ln(Ba/Ca) are generally within the range expected from the Rayleigh enrichment of these elements during ICD or PCP (Fig. S4a-b) (Fairchild and Treble, 2009; Sinclair, 2011; Wassenburg et al., 2024), but exceptions are found in the MIS 11b-c growth of samples 61D and 13. The clustering of data from individual stalagmites, which do not plot along a single enrichment line, reflects heterogeneities in host-rock composition and flow paths in different sections of the cave (Fig. S1).

Detritally sourced trace elements are generally coherent with each other and sulphide metals (especially in 60), with the notable exception of stalagmites 15D and 13 (Fig. S4d-e). There, a unique decoupling is observed among transition metals common to sulphides, whose mobility is enhanced by oxidising (Cu, Zn) or reducing (Fe, Mn, Ni) environments. Stalagmite 60 is the only sample for which S exhibits statistically significant covariance with other elements, and here it is positively correlated to minor cations (Mg, Sr, Ba), as well as Cu, Zn, and P.

Prior to ~392 ka, most trace elements have low concentrations, and heavier elements are commonly near the limit of detection. Between 372-365 ka, there is a distinct peak in cations from both

https://doi.org/10.5194/egusphere-2026-2840
Preprint. Discussion started: 16 June 2026


carbonate and clay minerals, sulphide-associated metals (including Fe and Ni but excluding Pb), and transition metals such as Co and Mn that are otherwise near detection limits. Importantly, this peak is not associated with any macroscopic features, such as 'dirty layers' or changes to the color or opacity of stalagmite 60, but it occurs just above the narrow bottleneck of the hourglass figure (Fig. S2) and corresponds to an interval of elevated growth rate.

To interpret speleothem geochemistry, concentrations of the same elements (plus Si) were measured in three host rock samples near the collection site of stalagmite 13 (Fig. S1). Host rock samples 1 and 2 are from massive limestone beds that represent the dominant lithology of the Quinten Formation, comprising bioclastic packstone and grainstone associated with deposition in the Late Jurassic carbonate platform (Weissert and Mohr, 1996). The mineralogy is predominantly micritic low-Mg calcite with low concentrations of sulphur (indistinguishable from background) and elements associated with siliciclastic detritus. Host rock sample 3 is from an intercalated shaly carbonate mudstone (marl) unit that is highly enriched in siliciclastic grains and contain a distinctly high sulphur content (15,000 µg/g) (Table S4).

## 4. Discussion

### *4.1 Global and local paleoclimate trends from MIS 11 to 10*

Marine Isotope Stage 11 (424–374 ka) was characterized by a pronounced and long climatic optimum lasting >18 kyr that followed the most extensive glaciation of the Middle Pleistocene (Milker et al., 2013; Tzedakis et al., 2022; Vera-Polo et al., 2024). Positive feedbacks associated with disintegration of the large ice sheets drove strong thermohaline circulation and marine warmth, particularly in the mid- to high-latitude North Atlantic (Hu et al., 2024; Milker et al., 2013). Anomalously high and sustained greenhouse-gas forcing, combined with weak orbital forcing of the low-eccentricity period, prevented glacial inception through the subsequent summer insolation minimum in the Northern Hemisphere (de Abreu et al., 2005; Nehrbass-Ahles et al., 2020; Tzedakis, 2010), which is nonetheless well expressed by precessionally driven contraction of the Asian Summer Monsoon system (Cheng et al., 2016). This delayed recovery of the polar cryosphere may partially be attributed to the out-of-phase relationship between precession and obliquity following peak warmth (Tzedakis et al., 2022), coupled with enhanced upwelling that drove $CO_2$ outgassing from the Southern Ocean and slowed global cooling (Jebasinski et al., 2026).

Marine records in the North Atlantic and Mediterranean document gradual cooling after ca. 400 ka, which broadly tracks the punctuated decline in atmospheric $CO_2$ (Milker et al., 2015) and is characterized by increasing millennial-scale variability in temperature and ice-rafted debris leading into MIS 10 (de Abreu et al., 2005; González-Lanchas et al., 2020; Oliveira et al., 2016; Oppo et al., 1998; Vázquez Riveiros et al., 2013). These trends and millennial-scale events are evident in the composite stable-isotope record from Betten Cave in the Swiss Alps (Fig. 2), which documents abrupt positive and extended negative excursions in $\delta^{18}O$, attributed respectively to

https://doi.org/10.5194/egusphere-2026-2840
Preprint. Discussion started: 16 June 2026


343 interstadial and stadial type perturbations to the ocean-cryosphere system of the high-latitude
344 Northern Hemisphere (see further discussion in Honiat et al., 2026). Collectively, these samples
345 span peak interglacial conditions during MIS 11c through a stepwise glacial advance over the
346 adjacent valleys during MIS 11a-b into a fully developed MIS 10 glaciation (subglacial speleothem
347 growth), thereby offering a rare, well-resolved archive of environmental change in an alpine setting
348 on orbital and sub-orbital timescales.

349

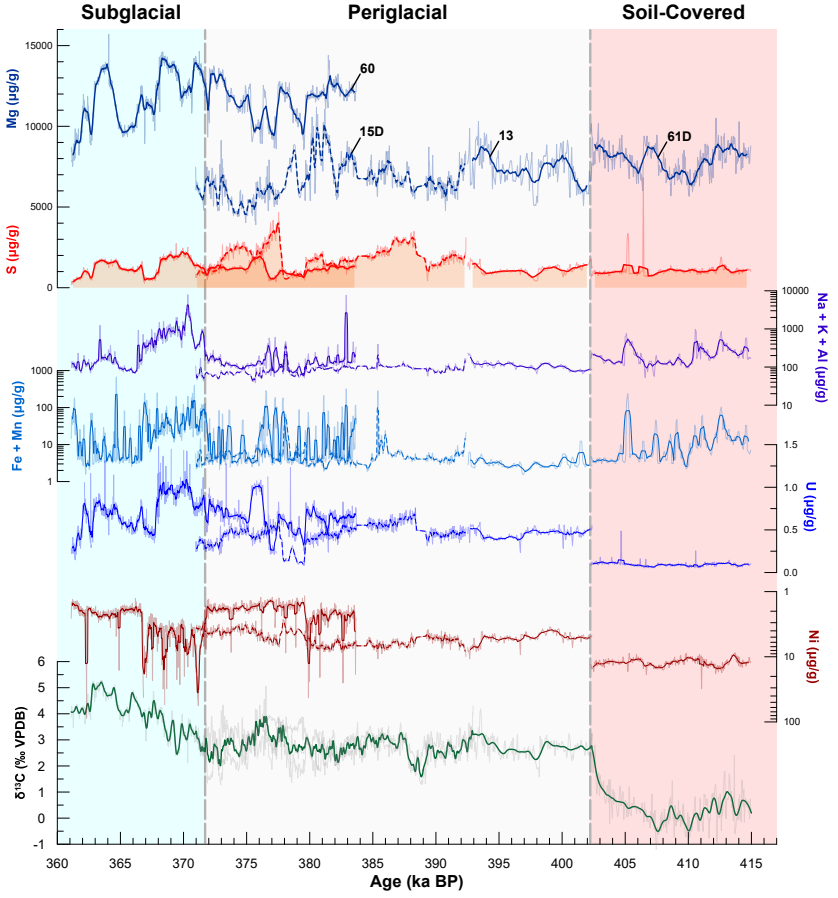


350

351 **Figure 3:** Environmental transitions during the MIS 11/10 glacial inception delineated from trace-element proxies.
352 Bold lines represent 15-point running means of elemental and isotope data (thin lines), plotted individually for
353 stalagmites 60, 15D, 13, and 61D. Spatial and/or stratigraphic heterogeneities in host-rock composition are evident
354 in systematic offsets between overlapping sections of 60 and 15D (dashed line), which were collected approximately
355 1 km horizontal and 300 m vertical distance from each other (Fig. S1). Note the inversion of vertical axes for Ni and
356 $\delta^{13}C$.

https://doi.org/10.5194/egusphere-2026-2840
Preprint. Discussion started: 16 June 2026


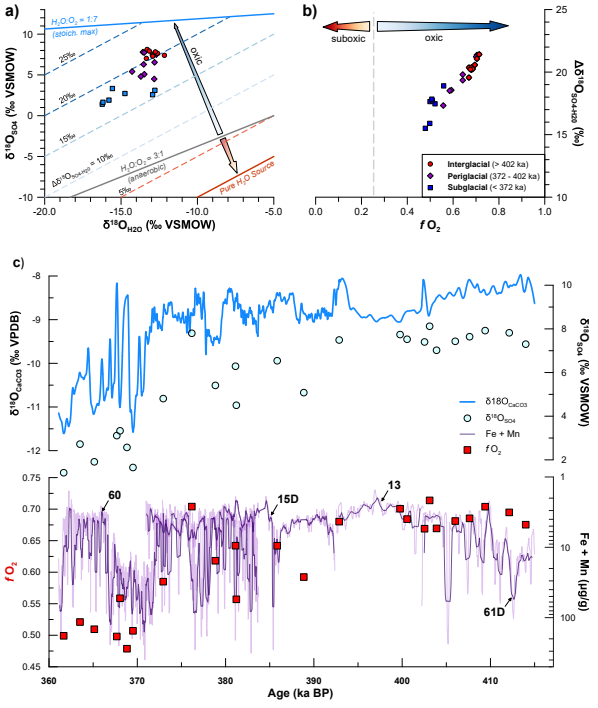


**Figure 4:** Environmental evolution of the Melchsee Frutt region during the MIS 11/10 glacial inception, interpreted from the oxygen-isotope composition of speleothem sulphate ($\delta^{18}O_{SO4}$). a) Cross-plot of $\delta^{18}O$ in sulphate ($\delta^{18}O_{SO4}$) and water ($\delta^{18}O_{H2O}$), estimated from the equilibrium dripwater equivalent of carbonate. Dashed lines follow constant isotopic offsets between sulphate and water $\Delta\delta^{18}O_{(SO4–H2O)}$. Bold blue and red lines indicate the stoichiometric limits from aerobic and anaerobic sulphide oxidation, respectively, assuming a fractionation of -8.7‰ from atmospheric $O_2$ (+23.8‰ VSMOW) and +4‰ from water during sulphide oxidation. Dark grey line marks the estimated threshold suggested by Bottrell (2007), below which anoxic conditions may be inferred. b) Cross plot of the fraction of sulphate oxygen derived from atmospheric O2 ($fO_2$) and the isotopic offset between sulphate and water $\Delta\delta^{18}O_{(SO4–H2O)}$. Dashed grey line marks the same threshold for anoxic environments. Speleothem data in (a) and (b) are color-coded by the inferred environment during the interglacial–glacial transition (see legend). Composite time series of c) carbonate $\delta^{18}O$; d) $\delta^{18}O_{SO4}$; e) $fO_2$; and f) uranium concentration, in µg/g (ppm) calcite.

### *4.2 Speleothem $\delta^{34}S_{SO4}$, $\delta^{13}C$, Ni, and U mark transition to periglacial environment at 402 ka*

An abrupt negative shift in speleothem $\delta^{34}S_{SO4}$ at 402 ± 3 ka, from +3.2‰ to −11.9‰, coincides with the marked increase in speleothem $\delta^{13}C$ from -1‰ to +3‰, indicating a fundamental reorganization of sulphur cycling concomitant with the increased contribution of host-rock carbon in place of soil-derived $CO_2$ (Fig. 2). Due to the wide natural range in $\delta^{34}S$ within marine systems (Canfield, 2004; Habicht and Canfield, 2001), the sulphur-isotope signal of $[SO_4^{2-}]$ in karst waters is highly sensitive to sulphate source, which may include atmospheric deposition, soil organic sulphur, carbonate-associated sulphate, and the oxidative weathering of sulphide minerals in the bedrock or catchment (Dogramaci et al., 2017; Szynkiewicz et al., 2012). These sources are

https://doi.org/10.5194/egusphere-2026-2840
Preprint. Discussion started: 16 June 2026


typically isotopically distinct: atmospheric, soil- and carbonate-derived sulphate tends to have higher $\delta^{34}S$ values (commonly near +15‰ in Jurassic–Cretaceous strata; Kampschulte and Strauss, 2004), whereas sedimentary sulphides may be strongly depleted in $^{34}S$ and yield low $\delta^{34}S$ values that typically reflect isotopic fractionation from the bacterial reduction of [$SO_4^{2-}$] in suboxic marine substrates (Habicht and Canfield, 2001). Importantly, sulphur-isotope fractionation during sulphide oxidation and subsequent aqueous transformations is generally small, such that the $\delta^{34}S$ of dissolved sulphate closely reflects that of its source (Bottrell, 2007; Taylor and Wheeler, 1993). Thus, we interpret the shift in speleothem $\delta^{34}S_{SO4}$ to reflect the onset of extensive sulphide oxidation and a SAD-dominated system in the absence of soil and increased presence of oxidants in the form of either dissolved $O_2$ or $Fe^{3+}$.

In isolation, the co-occurrence of low $\delta^{34}S_{SO4}$ and elevated $\delta^{13}C$ is consistent with both soil-free subglacial and soil-limited periglacial environments, in which biological inputs are minimized and oxidative weathering is enhanced. The seasonal infiltration of oxygenated meltwaters with low dissolved loads, whether from the glacier surface via moulins or in downstream runoff (Bottrell and Tranter, 2002; Zarroca et al., 2021), is particularly effective at oxidising sulphide phases and generating elevated sulphate concentrations. Although speleothem S concentration only increases slightly across this transition (Fig. 3), the increase in aqueous [$SO_4^{2-}$] must have been higher to offset the reduction in S expected from the halving of speleothem growth rates (Borsato et al., 2015; Wynn et al., 2018). However, the absence of trace-element signals indicative of glacial weathering and the fact that $\delta^{13}C$ stabilizes around +3‰ after 402 ka (nearly identical to host-rock values) more plausibly reflects the downstream input of glacial runoff to the karst aquifer, with the possibility of thin patchy soils above the cave site (Fig. 3). The geographic setting of Betten Cave is conducive to this scenario, because local glaciation would initiate at higher elevation and later advance through the Melchsee Frutt valley to the south(east), while the cave itself is hosted beneath a glacially carved ridge that separates Melchsee Frutt from the lower valley (Fig. 5; Fig. S1).

Abrupt and opposing shifts in speleothem Ni and U concentrations at 402 ka potentially hint at redox changes associated with the environmental transition (Fig. 4), although site-specific controls likely play a role. High Ni and low U from 415–402 ka indicate a more reducing environment, in which $Ni^{2+}$ mobilization and transport is favoured through aqueous and soil colloidal phases (especially in humic acids and goethite) and dissolved transport of uranyl ions is strongly inhibited (Fairchild and Treble, 2009; Rinklebe and Shaheen, 2017). Whilst most soil environments are oxidising, microbial respiration and oxidation of organic matter reduce $O_2$ availability in the presence of sulphate and can plausibly restrict redox potential relative to a bare-rock SAD environment, promoting the prior co-precipitation of U in the epikarst. This process may also be reflected in the negative correlation between U concentration and initial $^{234}U/^{238}U$ activity ratio observed in the stalagmites comprising our speleothem composite (Fig. S6), although we caution that spatial heterogeneity in the cave system is observed to contribute strongly to this variance. Low U concentrations during the initial growth phase correspond to exceptionally high $UAR_{(i)}$

https://doi.org/10.5194/egusphere-2026-2840
Preprint. Discussion started: 16 June 2026


from 4.8–5.4, which must reflect strong fractionation from alpha-recoil of $^{234}$Th into groundwater. Given the higher growth rates of stalagmite 61D (Fig. S2; Honiat et al., 2026), these effects are not likely explained by increased residence time and water-rock interaction relative to subsequent phases. However, limited U mobility under reducing conditions, which promotes the prior precipitation of U, can amplify alpha-recoil effects through recycling of aqueous uranyl, despite strong recharge of the system suggested by high growth rate and low minor cations (Fig. 3; Fig. S4).

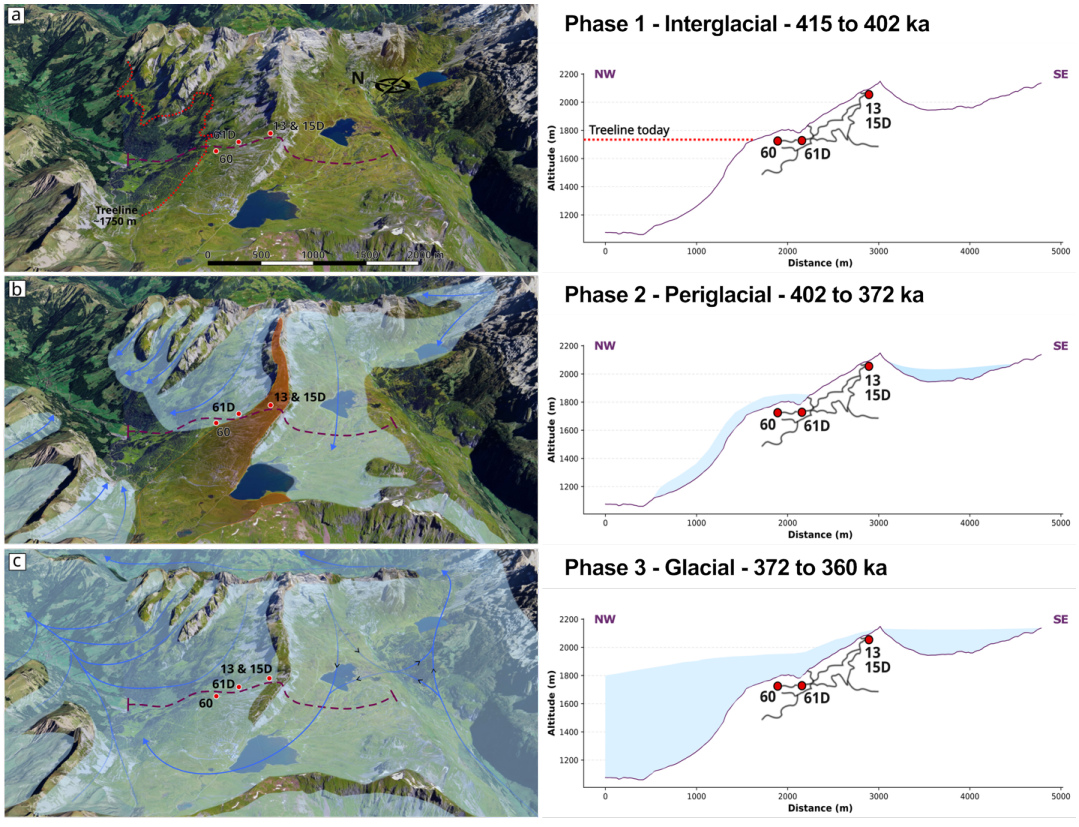


**Figure 5:** Conceptual evolution of the alpine ice margin during the MIS 11/10 glacial inception. a) From 415–402 ka, ice-free interglacial conditions prevail, similar to modern. Soils are present, but only stalagmite 61D is actively growing, possibly within the tree line. The modern limit at ~1750 m a.s.l. is shown by the red dashed line. b) From 402–372 ka, growth of 61D ceases, while stalagmites 13 and then 15D become active, likely under the influence of glacial meltwater to the aquifer that promoted sulphide oxidation. The ice margin reaches the upper valley (~2000 m a.s.l.) at the beginning of this stage. Growth of stalagmite 60 begins late in the stage, plausibly when warm-based ice flow from the northeast reaches the local surface elevation (1800 m a.s.l.). c) From 372–360 ka, the temperate glacier thickens and spills over the ridge to reach the lower valley. Fully subglacial conditions characterize the surface above stalagmite 60, while growth in 13 and 15D ceases between 372–370 ka, possibly in connection with a cold-based glacier margin. Maps data: © Google Earth 2026; images: © Landsat / Copernicus, Maxar Technologies.

https://doi.org/10.5194/egusphere-2026-2840
Preprint. Discussion started: 16 June 2026


Following 402 ka, U concentration abruptly increases and $UAR_{(i)}$ decreases, while Ni falls to values near the analytical detection limit. We interpret these trends to reflect a reduction in soil influence and contribution of oxidising glacial runoff to the aquifer, which promotes the oxidation of sulphide minerals to a degree that dominates the aqueous sulphate source. Although this interpretation is ostensibly at odds with the strong mobilization of Ni during sulphide oxidation (Brighenti et al., 2025), Fe- and Mn-(oxyhydro)oxides precipitated under persistently oxidising conditions are highly effective at scavenging $Ni^{2+}$ in the groundwater (Frierdich and Catalano, 2012), which is more likely during long transport from an upstream glacier terminus. The stability of elemental and isotopic signals through the remainder of this phase indicates that the ice margin may have remained in the upper valley until ~372 ± 3 ka (Fig. 5b).

### *4.3 Speleothem $\delta^{18}O_{SO4}$ tracks oxygen limitation during cooling and glacial advance*

The oxygen-isotope composition of aqueous sulphate ($\delta^{18}O_{SO4}$) provides additional constraints on sulphur sources, reactive pathways of sulphide oxidation, and the redox potential of the system (Bottrell, 2007; Wynn et al., 2006, 2015). Although sulphide oxidation can be limited by the availability of dissolved $O_2$ (Eq. 1), the reaction may proceed anaerobically via oxidants such as $Fe^{3+}$ (Equation 3) (Wadham et al., 2007). Stoichiometrically, between 12.5 and 100% of sulphate oxygen derives from $H_2O$, depending on the pathway (Bottrell, 2007; Taylor and Wheeler, 1993):

$$FeS_2 + \frac{7}{2}O_2 + H_2O \rightarrow Fe^{2+} + 2\,SO_4^{2-} + 2\,H^+ \quad (1)$$

$$Fe^{2+} + \frac{1}{4}\,O_{2(aq)} + H^+ \rightarrow Fe^{3+} + \frac{1}{2}\,H_2O \quad (2)$$

$$FeS_2 + 14\,Fe^{3+} + 8\,H_2O \rightarrow 15\,Fe^{2+} + 2\,SO_4^{2-} + 16\,H^+ \quad (3)$$

Due to the large difference in $\delta^{18}O$ between atmospheric oxygen (+23.8‰) and meteoric recharge in an alpine karst system (less than -8‰), the final $\delta^{18}O_{SO4}$ is highly sensitive to the source ratio of sulphate oxygen. Given the typical isotopic fractionation from $O_2$ ($\varepsilon_{O2}$ = -8.7‰) and water ($\varepsilon_{H2O}$ = 0 to 4‰) during sulphide oxidation, $\delta^{18}O_{SO4}$ may be quantified as a mass balance equation:

$$\delta^{18}O_{SO4} = f\,O_2 \cdot (23.8‰ + \varepsilon_{O2}) + (1 - f\,O_2) \cdot (\delta^{18}O_{H2O} + \varepsilon_{H2O}) \quad (4)$$

Where $fO_2$ is the molar fraction of sulphate oxygen derived from atmospheric $O_2$. Under fully oxidising environments, equation (1) dominates ($fO_2$ = 0.875), and the aerobic oxidation of sulphide leads to high $\delta^{18}O_{SO4}$ values that approach that of atmospheric oxygen minus a fractionation factor that depends on the sterility of the environment in terms of iron-oxidising

https://doi.org/10.5194/egusphere-2026-2840
Preprint. Discussion started: 16 June 2026


bacteria (-4.3 to -11.2‰) (Taylor and Wheeler, 1993). In the absence of $O_2$, however, available $Fe^{3+}$ allows equation (3) to proceed and cause $\delta^{18}O_{SO4}$ to approach that of the water. Thus, the redox state of the environment at the point of sulphate production may be reflected in the isotopic offset between $\delta^{18}O$ of the sulphate and water ($\Delta\delta^{18}O_{SO4\text{-}H2O}$).

The main limitation to this approach is that equation (4) assumes no isotopic exchange between sulphur species and water, which would lead to much lower $\delta^{18}O_{SO4}$ despite an atmospheric source (Bottrell, 2007). Although $SO_4$ is stable on geologic timescales and resilient to isotopic exchange, oxidation proceeds via intermediate species ($SO_3^{2-}$ and $SO_2(OH)^-$), for which the rate of isotopic exchange typically exceeds the rate of oxidation to $SO_4$ by an order of magnitude (Betts and Voss, 1970). In light of this dual control, Bottrell and Tranter (2002) proposed that the threshold for identifying sulphide oxidation in an anoxic environment corresponds to an $fO_2$ of 0.25 or $H_2O$:$O_2$ ratio of 3:1 (Fig. 4a). For data plotting above this anoxia threshold (Fig. 4a-b), we cannot distinguish between effects of water exchange and oxygen availability on $\Delta\delta^{18}O_{SO4\text{-}H2O}$.

Speleothem sulphate data from this study consistently plot well above the anoxia threshold in the $\delta^{18}O_{SO4}$ vs. $\delta^{18}O_{H2O}$ space (Fig. 4a), corresponding to $fO_2$ fractions between 0.48–0.72 and suggesting high oxygen availability during sulphide oxidation (Fig. 4b; Table S3). However, there is a distinct negative trend following the statistical break point near 400 ka, after which $\Delta\delta^{18}O_{SO4\text{-}H2O}$ declines from +22‰ to +15‰, possibly tracking long-term oxygen limitation (Fig. 2b). This trend was hypothesized by Spötl et al. (2024) to occur during glacial advance as the environment transitioned from a well-oxygenated ice-marginal system to being covered by a progressively thickening warm-based glacier with limited hydrological connectively to surface melts (Skiba et al., 2023b). Modern observations of subglacial discharge have documented oxygen-limited to suboxic conditions—particularly during winter—leading to low $\delta^{18}O_{SO4}$ values (Bottrell and Tranter, 2002; Wadham et al., 2007; Wynn et al., 2006, 2015), but this phenomenon has never been documented for a paleo-glacier setting.

To interpret the negative trend in $\Delta\delta^{18}O_{SO4\text{-}H2O}$ from 402 to 360 ka (Fig. 4c), we consider two scenarios with boundary assumptions that (1) no isotopic exchange occurred between water and sulphate intermediaries; or (2) sulphide oxidation remained fully aerobic ($fO_2$ = 0.875) but with variable water exchange:

1) $fO_2$ decreases from ~0.72 (MIS 11c) to ~0.48 (MIS 10), with the lowest values following the breakpoint in speleothem $\delta^{18}O$ near 372 ± 3 ka (Fig. 4c). This trend is consistent with increasingly anaerobic sulphide oxidation during glacial advance or thickening, due to reduced $O_2$ availability and an increase in Fe3+ to sustain microbial communities (Sharp et al., 1999).
2) The fraction of equilibrium exchange with water steadily increased from MIS 11c to MIS 10, due kinetic changes in the hydrochemical environment.

https://doi.org/10.5194/egusphere-2026-2840
Preprint. Discussion started: 16 June 2026


Although the latter parameter is unlikely to trend over time in a well-buffered carbonate system, several kinetic factors are coupled to glacial advance. First, more aggressive sulphide oxidation near the ice-rock interface (Fig. 6a-b) can lead to a localized decrease (increase) in pH (aqueous $[SO_4^{2-}]$), which can exponentially increase the rate of isotopic exchange with water (Betts and Voss, 1970). Secondly, enhanced water storage and longer residence times in subglacial melts could lead to localized or seasonal anoxia (Wadham et al., 2007; Wynn et al., 2006) (Fig. 6c-d), reducing the oxidation rate of intermediaries to stable $SO_4^{2-}$. Finally, isotopic exchange is promoted by microbial mediation (Bottrell, 2007), and these bacteria contribute strongly to glacial chemical weathering (Montross et al., 2013; Sharp et al., 1999).

Importantly, these scenarios are complementary and not mutually exclusive. Despite uncertainties in the oxygen source and reactive pathways, we conclude that the trend in $\Delta\delta^{18}O_{SO4\text{-}H2O}$ robustly captures the advance and thickening of a warm-based glacier through the Melchsee Frutt valley during late MIS 11 and early MIS 10. Combining this with evidence from $\delta^{34}S_{SO4}$, we contend that the glacier terminus was sufficiently proximal to Betten Cave to dominate hydrological inputs no later than 402 ± 4 ka, and the cave environment became fully subglacial no later than 372 ± 3 ka (Fig. 5b-c).

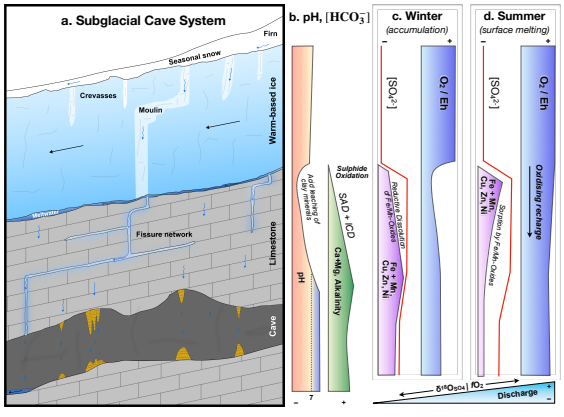


**Figure 6:** Conceptual geochemical evolution of the subglacial speleothem system from the glacier surface to the stalagmite. a) Schematic cross section of the subglacial environment. b) Vertical changes in pH, cations, and carbonate alkalinity. Meltwater pH begins slightly acidic, due to atmospheric mixing, but falls abruptly in response to sulphide oxidation at the glacier-rock interface. Neutralization is facilitated by sulphuric-acid dissolution of carbonate host rock, which generates aqueous-phase cations and carbonate alkalinity, so that calcite saturation (and precipitation) is achieved within the vadose zone. c) Winter geochemical pathway: reduced discharge limits redox potential of subglacial meltwater, and sulphide oxidation (preferring the anaerobic pathway) generates sulphate and associated transition metals; reductive dissolution of Fe/Mn-(oxyhydr)oxides keeps metals in solution. d) Summer geochemical pathway: melting of the glacier surface provides oxidising recharge, raising redox potential; transition metals generated by sulphide oxidation (preferring the aerobic pathway) are captured by Fe/Mn-(oxyhydr)oxides as $Fe^{2+}$ is oxidised to $Fe^{3+}$, limiting mobility.

https://doi.org/10.5194/egusphere-2026-2840
Preprint. Discussion started: 16 June 2026


*4.4 Onset of subglacial conditions captured by redox cycling of trace metals*

Trace-element systematics in speleothem calcite reflect hydrological, weathering, and redox controls (Fairchild and Treble, 2009). At transient intervals from ~392–372 ka and especially following 372 ± 3 ka, abrupt increases in minor cations (Mg, Sr, and Ba) and detrital elements (Fig. 3) may be attributed to the enhanced delivery of glacially comminuted detritus from the advance of a warm-based glacier over the cave site (Fortner et al., 2011; Hawkings et al., 2025; Prestrud Anderson et al., 1997; Stachnik et al., 2016) (Fig. 6). Elevated minor cations in this phase cannot be attributed solely to Rayleigh enrichment from PCP, due to molar limitations of bicarbonate in a SAD-dominated system (Sect. 2.3). However, a common weathering control on Mg, Sr, Ba and S is produced by the exposure of highly reactive grain surfaces (Graly et al., 2018; Wadham et al., 2010), especially from the less soluble marl interbeds that are rich in these elements (Sect. 2.4), which results in strong cation enrichment via ICD and simultaneously the enhanced oxidative weathering of sulphides (Fig. S3e) (Hodson et al., 2016; McGillen and Fairchild, 2005; Williams et al., 2006). This interpretation is corroborated by the unique relationships between sulphide-associated metals and siliciclastic 'detrital' elements during late MIS 11 and MIS 10 (Fig. S5). Deviations from simple mixing lines with the host rock, expected from varying colloidal transport and inclusion, are parsimoniously explained by acid-leaching of K and Na from clay minerals and the transient recycling of redox-sensitive elements.

Distinct redox controls are evident in the geochemical parameters affecting U and Ni mobility along the karst flow path. Under oxidising conditions, U is present as soluble uranyl complexes and efficiently transported and incorporated into calcite (Fairchild and Treble, 2009). In contrast, Ni mobility is strongly influenced by pH and, critically, by adsorption–desorption reactions with Fe- and Mn-(oxyhydr)oxides (Liu et al., 2022; Singh et al., 1984). During initial sulphide oxidation, $Fe^{3+}$ produced in solution precipitates as Fe-(oxyhydr)oxides, which act as highly effective scavengers for Ni and other transition metals (e.g., Co, Cu, Zn) (Frierdich and Catalano, 2012; Singh et al., 1984), thereby depleting dissolved Ni along the flow path while allowing U to remain mobile (Fig. 6d). This fundamental decoupling leads to the observed inverse relationship between U and Ni prior to ~392 ka (Fig. 3); however, subsequent intervals (especially ~372–360 ka) are characterized by positive covariance of Ni with U and S, indicating a transient breakdown of the decoupling that may explained by the seasonally distinct redox states characteristic of subglacial environments in which sulphide oxidation is prevalent (Fig. 6c-d) (Graly et al., 2018; Hawkings et al., 2025; Hubbard and Nienow, 1997; Wynn et al., 2006).

Millennial-scale pulses of higher $\delta^{18}O$ in calcite, superimposed on an orbital-scale cooling trend, are interpreted as warmer conditions analogous to Dansgaard-Oeschger interstadials and enhanced meltwater from the glacier surface (Fohlmeister et al., 2023; Honiat et al., 2026; Skiba et al., 2023a). High Ni during these pulses is accompanied by enrichments in a suite of redox-sensitive and trace elements (Fe, Mn, Cu, Co, Na, K, P, Ba, and U), which are known to concentrate in Mn oxides in cave systems (Frierdich et al., 2011), and such co-enrichment strongly points to the

https://doi.org/10.5194/egusphere-2026-2840
Preprint. Discussion started: 16 June 2026


remobilization of metals sequestered under more oxidising conditions (Liu et al., 2022). One plausible mechanism is the reductive dissolution of Fe/Mn-(oxyhydr)oxides during winter, which releases sorbed trace metals back into solution (Frierdich et al., 2011; Liu et al., 2022; Singh et al., 1984). This process may be driven by seasonally suboxic conditions beneath the glacier (Fig. 6), particularly if an excess of $Fe^{3+}$ is produced via Eq. (2), due to aggressive sulphide oxidation following the oxidising recharge of surface melts, which may remain elevated over millennial timescales (Skiba et al., 2023a).

Sulphur isotope systematics indicate a complementary shift in sulphide oxidation pathway. The observed trend toward low $\Delta\delta^{18}O_{SO4\text{-}H2O}$, which reaches local minima during MIS 10 interstadials, suggests that progressively less $O_2$ contributed to sulphate oxygen (i.e. $Fe^{3+}$ acted as the primary oxidant). The $Fe^{3+}$ required for this process is sustained by ongoing redox cycling in the presence of strong glacial weathering, Fe production from sulphide oxidation, and coupling to Mn oxides (Hodson et al., 2016; Liu et al., 2022). $Fe^{2+}$ released during reductive dissolution can be re-oxidised to $Fe^{3+}$ during seasonal flushing of surface melts, maintaining a dynamic redox loop (Fig. 6c-d).

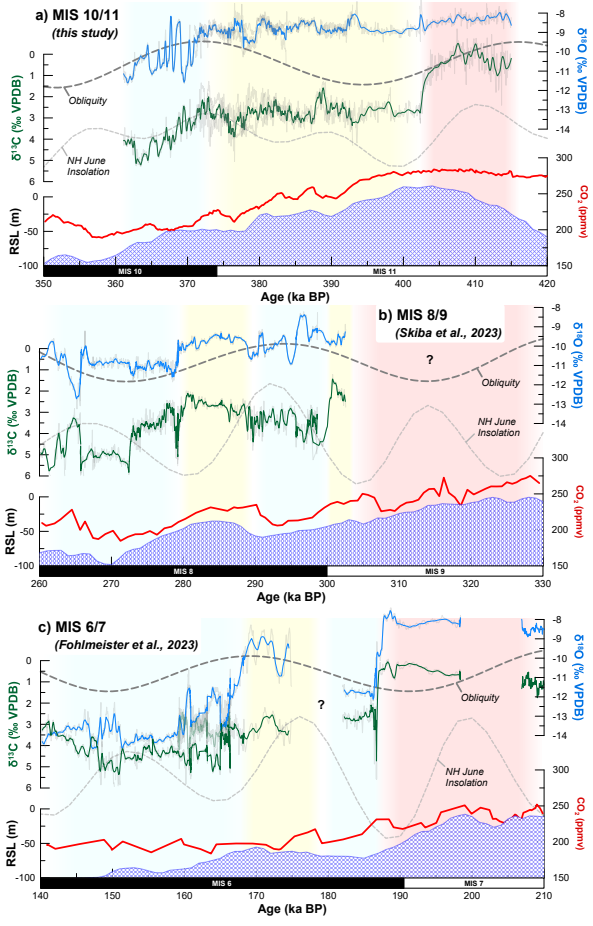

https://doi.org/10.5194/egusphere-2026-2840
Preprint. Discussion started: 16 June 2026


**Figure 7:** Climate dynamic thresholds of glacial inception in the NW Alps constrained by speleothems in the Melchsee Frutt region. Shading refers to interpreted environments: soil-influenced interglacial (red); soil-limited periglacial transition (yellow); soil-free subglacial (blue). Obliquity (dashed lines) and Northern Hemisphere June insolation (dotted lines) are scaled arbitrarily for reference. Atmospheric $CO_2$ (Lüthi et al., 2008; Nehrbass-Ahles et al., 2020) is shown by the red line, and sea level (Spratt and Lisiecki, 2016) is given by the blue cross-hatched areal curve. a) MIS 10/11 glacial inception (Honiat et al., 2026), with environmental transitions corresponding to those in Figure 3. Transitions during the MIS 8/9 (b) and MIS 6/7 (c) glacial inceptions are tentatively constrained by speleothem $\delta^{13}C$ and $\delta^{18}O$ alone (Skiba et al., 2023a; Fohlmeister et al., 2023).

### *4.5 Timing of alpine glacial inception is modulated by greenhouse and ice-sheet forcing*

In previously published records from caves in the Melchsee Frutt karst (Fohlmeister et al., 2023; Skiba et al., 2023a), transient glaciation of the catchment between MIS 6–9 is primarily diagnosed from speleothem $\delta^{13}C$ relative to the host-rock value (+2.7‰). The bimodal clustering of $\delta^{13}C$ and $\delta^{18}O$ and the covariance of elevated $\delta^{13}C$ with PCP-sensitive cations (Mg and Sr) are similarly observed in our composite MIS 11/10 record (Fig. S4; Honiat et al., 2026). However, we find evidence from novel proxies for a transitional periglacial phase (Fig. 5b), in which speleothem $\delta^{13}C$ stabilises near that of the host rock, and $\delta^{18}O$ more closely resembles interglacial values.

If we apply this framework to records spanning the MIS 9/8 and MIS 7/6 glacial inceptions (Fig. 7), it suggests that MIS 11a-b was characterized by a uniquely long-lasting intermediate phase, whereas subsequent glacial inceptions were relatively abrupt. Additionally, there may have been interstadial rebounds during early MIS 8 (280–290 ka) and 6 (168-176 ka), in which climatic amelioration allowed for ice retreat to the upper Melchsee Frutt valley (i.e. above 2,000 m a.s.l.; Fig. 5). We caution that this preliminary interpretation is contingent on finding elemental and isotopic signals analogous to those documented herein—if we could apply the same multiproxy analysis to all transitions in Figure 7—and thus it simultaneously presents a series of hypotheses to be tested in future work.

Crucially, Melchsee Frutt speleothems exhibit the strongest stable-isotope evidence for subglacial conditions below threshold levels of atmospheric $CO_2$ (200-225 ppmv) and relative eustatic change (below -25 m)—the latter a recorder of continental ice extent. Conversely, glacial inceptions are not consistently in phase with orbital forcing, as they can occur during both maxima and minima in obliquity and insolation (Fig. 7). This discrepancy highlights the strong sensitivity of mountain glacier dynamics to greenhouse forcing and ice-sheet configurations, with the latter modulating synoptic air circulation and associated moisture sources over Europe (Fig. S7). From the perspective of past climate dynamics, our paleo-glacier record thus corroborates the observed and forecasted retreat of alpine glaciation in response to unprecedented greenhouse forcing and disintegration of the polar cryosphere.

## 5. Conclusions

https://doi.org/10.5194/egusphere-2026-2840
Preprint. Discussion started: 16 June 2026


Our multiproxy record resolves a three-phase environmental transition across the MIS 11/10 glacial inception in the Melchsee Frutt region. From 415–402 ka, stable-isotope proxies of $\delta^{13}C$ (below +3‰), $\delta^{18}O$ (above -9‰), $\delta^{34}S_{SO4}$ (+3.2‰), and $\delta^{18}O_{SO4}$ (~7–8‰) indicate limited sulphide oxidation under a soil-influenced meteoric recharge regime. Along with trace elements, these signals align with those typical of a warm interglacial setting. An abrupt shift at 402 ± 4 ka marks the onset of extensive sulphide oxidation: $\delta^{34}S_{SO4}$ falls to −12‰ as $\delta^{13}C$ rises to host-rock values. Trace elements and elevated $\delta^{18}O_{SO4}$ point to an oxidising environment that is best explained by glacial runoff feeding the karst and scavenging transition metals on Fe–Mn oxides during transport. Concurrently, $\Delta\delta^{18}O_{SO4-H2O}$ begins a long-term decline, signalling greater incorporation of water-derived oxygen into sulphate and progressive oxygen limitation as ice thickens and advances through the upper Melchsee Frutt valley (>2000 m a.s.l.). By 372 ± 3 ka, persistently high $\delta^{13}C$ above host-rock values and a breakpoint toward lower $\delta^{18}O$ indicate subglacial speleothem growth beneath a warm-based glacier, whose terminus extended below 1,700 m a.s.l. Trace-element peaks in cations and redox-sensitive metals reflect enhanced delivery of glacially comminuted detritus, incongruent calcite dissolution of marl interbeds, and coupled Fe-Mn redox cycling that remobilizes scavenged metals—hallmarks of subglacial hydrology and weathering regimes.

The reconstruction of mountain glaciers beyond the Last Glacial Maximum has long been inhibited by preservation bias against montane landforms and the limited chronological precision of alpine foreland deposits. We contend that the multiproxy approach presented herein can overcome these barriers, allowing for the precise reconstruction of mountain glacier dynamics from alpine speleothems, plausibly back to the Early Pleistocene onset of glaciation for the European Alps. These methods should be applicable to mountainous karst regions around the world, which may record much longer ice histories. Robust constraints on the timing of glacier advance and retreat through specific elevations further provide a powerful metric to calibrate and validate palaeomodelling and forecasts of the alpine cryosphere.

## Data availability

All data necessary to replicate the results presented in this study are provided in Supplementary Tables S1, S2, S3, and S4, available online at https://doi.org/10.5281/zenodo.20259664.

## Author Contributions

JLB, CS, and PMW designed the study and together with RMK performed laboratory and formal analysis. CS, MT, AH, JF, and JLB conducted fieldwork. SH conducted proxy system modelling. JR performed site-level climate model extraction and formal analysis. JLB, AH, PMW, and CS prepared the original draft, and all authors contributed to subsequent review and editing. CS was responsible for funding acquisition and together with RLE contributed resources and methodology.

https://doi.org/10.5194/egusphere-2026-2840
Preprint. Discussion started: 16 June 2026


## Competing Interests

The authors declare that they have no conflict of interest.

## Acknowledgements

The authors thank Dave Hughes (Lancaster Environment Centre) for laboratory support and data processing related to the isotopic analysis of sulphate.

## Financial Support

This research has been funded in whole or in part by the Austrian Science Fund (FWF) (grant DOI https://doi.org/10.55776/P35877, project no. P35877).

https://doi.org/10.5194/egusphere-2026-2840
Preprint. Discussion started: 16 June 2026


## LaTeX Code for Equations

**Equation 1:** \mathrm{FeS_2} + \frac{7}{2}\,\mathrm{H_2O} \rightarrow \mathrm{Fe^{2+}} + 2\,\mathrm{SO_4^{2-}} + 2\,\mathrm{H^+}

**Equation 2:** \mathrm{Fe^{2+}} + \frac{1}{4}\,\mathrm{O_{2(aq)}} + \mathrm{H^+} \rightarrow \mathrm{Fe^{3+}} + \frac{1}{2}\,\mathrm{H_2O}

**Equation 3:** \mathrm{FeS_2} + 14\,\mathrm{Fe^{3+}} + 8\,\mathrm{H_2O} \rightarrow 15\,\mathrm{Fe^{2+}} + 2\,\mathrm{SO_4^{2-}} + 16\,\mathrm{H^+}

**Equation 4:** \mathrm{\delta^{18}O_{SO4}} = f\mathrm{O_2}\cdot \mathrm{(23.8‰ + \varepsilon_{O2})} + (1-f\mathrm{O_2})\cdot(\mathrm{\delta^{18}O_{H2O} + \varepsilon_{H2O}})

https://doi.org/10.5194/egusphere-2026-2840
Preprint. Discussion started: 16 June 2026


## References Cited

de Abreu, L., Abrantes, F. F., Shackleton, N. J., Tzedakis, P. C., McManus, J. F., Oppo, D. W., and Hall, M. A.: Ocean climate variability in the eastern North Atlantic during interglacial marine isotope stage 11: A partial analogue to the Holocene?, Paleoceanography, 20, https://doi.org/10.1029/2004PA001091, 2005.

Bajo, P., Borsato, A., Drysdale, R., Hua, Q., Frisia, S., Zanchetta, G., Hellstrom, J., and Woodhead, J.: Stalagmite carbon isotopes and dead carbon proportion (DCP) in a near-closed-system situation: An interplay between sulphuric and carbonic acid dissolution, Geochim. Cosmochim. Acta, 210, 208–227, https://doi.org/10.1016/j.gca.2017.04.038, 2017.

Bajo, P., Drysdale, R. N., Woodhead, J. D., Hellstrom, J. C., Hodell, D., Ferretti, P., Voelker, A. H. L., Zanchetta, G., Rodrigues, T., Wolff, E., Tyler, J., Frisia, S., Spötl, C., and Fallick, A. E.: Persistent influence of obliquity on ice age terminations since the Middle Pleistocene transition, Science (1979)., 367, 1235–1239, https://doi.org/10.1126/science.aaw1114, 2020.

Betts, R. H. and Voss, R. H.: The kinetics of oxygen exchange between the sulfite ion and water, Can. J. Chem., 48, 2035–2041, https://doi.org/10.1139/v70-339, 1970.

Boch, R., Cheng, H., Spötl, C., Edwards, R. L., Wang, X., and Häuselmann, Ph.: NALPS: a precisely dated European climate record 120–60 ka, Climate of the Past, 7, 1247–1259, https://doi.org/10.5194/cp-7-1247-2011, 2011.

Borsato, A., Frisia, S., Wynn, P. M., Fairchild, I. J., and Miorandi, R.: Sulphate concentration in cave dripwater and speleothems: Long-term trends and overview of its significance as proxy for environmental processes and climate changes, Quat. Sci. Rev., 127, 48–60, https://doi.org/10.1016/j.quascirev.2015.05.016, 2015.

Bottrell, S. H.: Stable isotopes in aqueous sulphate as tracers of natural and contaminant sulphate sources: A reconnaissance study of the Xingwen karst aquifer, Sichuan, China, Geol. Soc. Spec. Publ., 279, 123–135, https://doi.org/10.1144/SP279.11, 2007.

Bottrell, S. H. and Tranter, M.: Sulphide oxidation under partially anoxic conditions at the bed of the Haut Glacier d'Arolla, Switzerland, Hydrol. Process., 16, 2363–2368, https://doi.org/10.1002/hyp.1012, 2002.

Brighenti, S., Bearzot, F., Delpero, M., Tirler, W., Tolotti, M., Vorhauser, S., Bachmann, C., Romanin, E., Sparber, K., Vidoni, B., Fogale, F., and Comiti, F.: Increasing Nickel Concentrations in a Large River Network of South Tyrol, Eastern European Alps, ACS ES&T Water, 5, 594–604, https://doi.org/10.1021/acsestwater.4c00587, 2025.

Canfield, D. E.: The evolution of the Earth surface sulfur reservoir, Am. J. Sci., 304, 839–861, https://doi.org/10.2475/ajs.304.10.839, 2004.

https://doi.org/10.5194/egusphere-2026-2840
Preprint. Discussion started: 16 June 2026


Cheng, H., Edwards, R. L., Sinha, A., Spötl, C., Yi, L., Chen, S., Kelly, M., Kathayat, G., Wang, X., Li, X., Kong, X., Wang, Y., Ning, Y., and Zhang, H.: The Asian monsoon over the past 640,000 years and ice age terminations, Nature, 534, 640–646, https://doi.org/10.1038/nature18591, 2016.

Clauzel, L., Ménégoz, M., Gilbert, A., Gagliardini, O., Six, D., Gastineau, G., and Vincent, C.: Sensitivity of Glaciers in the European Alps to Anthropogenic Atmospheric Forcings: Case Study of the Argentière Glacier, Geophys. Res. Lett., 50, https://doi.org/10.1029/2022GL100363, 2023.

Colombo, N., Salerno, F., Martin, M., Malandrino, M., Giardino, M., Serra, E., Godone, D., Said-Pullicino, D., Fratianni, S., Paro, L., Tartari, G., and Freppaz, M.: Influence of permafrost, rock and ice glaciers on chemistry of high-elevation ponds (NW Italian Alps), Science of The Total Environment, 685, 886–901, https://doi.org/10.1016/j.scitotenv.2019.06.233, 2019.

Columbu, A., Sauro, F., Lundberg, J., Drysdale, R., and De Waele, J.: Palaeoenvironmental changes recorded by speleothems of the southern Alps (Piani Eterni, Belluno, Italy) during four interglacial to glacial climate transitions, Quat. Sci. Rev., 197, 319–335, https://doi.org/10.1016/j.quascirev.2018.08.006, 2018.

Cook, S. J., Jouvet, G., Millan, R., Rabatel, A., Zekollari, H., and Dussaillant, I.: Committed Ice Loss in the European Alps Until 2050 Using a Deep-Learning-Aided 3D Ice-Flow Model With Data Assimilation, Geophys. Res. Lett., 50, https://doi.org/10.1029/2023GL105029, 2023.

Dogramaci, S., McLean, L., and Skrzypek, G.: Hydrochemical and stable isotope indicators of pyrite oxidation in carbonate-rich environment; the Hamersley Basin, Western Australia, J. Hydrol. (Amst)., 545, 288–298, https://doi.org/10.1016/j.jhydrol.2016.12.009, 2017.

Fairchild, I. J. and Treble, P. C.: Trace elements in speleothems as recorders of environmental change, Quat. Sci. Rev., 28, 449–468, https://doi.org/10.1016/j.quascirev.2008.11.007, 2009.

Fairchild, I. J., Killawee, J. A., Hubbard, B., and Wolfgang Dreybrodt: Interactions of calcareous suspended sediment with glacial meltwater: a field test of dissolution behaviour, Chem. Geol., 155, 243–263, https://doi.org/10.1016/S0009-2541(98)00170-3, 1999.

Fiebig, M. and Preusser, F.: Pleistocene glaciations of the northern Alpine Foreland, Geogr. Helv., 63, 145–150, https://doi.org/10.5194/gh-63-145-2008, 2008.

Fohlmeister, J., Voarintsoa, N. R. G., Lechleitner, F. A., Boyd, M., Brandtstätter, S., Jacobson, M. J., and L. Oster, J.: Main controls on the stable carbon isotope composition of speleothems, Geochim. Cosmochim. Acta, 279, 67–87, https://doi.org/https://doi.org/10.1016/j.gca.2020.03.042, 2020.

Fohlmeister, J., Luetscher, M., Spötl, C., Schröder-Ritzrau, A., Schröder, B., Frank, N., Eichstädter, R., Trüssel, M., Skiba, V., and Boers, N.: The role of Northern Hemisphere summer

https://doi.org/10.5194/egusphere-2026-2840
Preprint. Discussion started: 16 June 2026


insolation for millennial-scale climate variability during the penultimate glacial, Commun. Earth Environ., 4, 245, https://doi.org/10.1038/s43247-023-00908-0, 2023.

Fortner, S. K., Mark, B. G., McKenzie, J. M., Bury, J., Trierweiler, A., Baraer, M., Burns, P. J., and Munk, L.: Elevated stream trace and minor element concentrations in the foreland of receding tropical glaciers, Applied Geochemistry, 26, 1792–1801, https://doi.org/10.1016/j.apgeochem.2011.06.003, 2011.

Frierdich, A. J. and Catalano, J. G.: Distribution and speciation of trace elements in iron and manganese oxide cave deposits, Geochim. Cosmochim. Acta, 91, 240–253, https://doi.org/10.1016/j.gca.2012.05.032, 2012.

Frierdich, A. J., Hasenmueller, E. A., and Catalano, J. G.: Composition and structure of nanocrystalline Fe and Mn oxide cave deposits: Implications for trace element mobility in karst systems, Chem. Geol., 284, 82–96, https://doi.org/10.1016/j.chemgeo.2011.02.009, 2011.

González-Lanchas, A., Flores, J.-A., Sierro, F. J., Bárcena, M. Á., Rigual-Hernández, A. S., Oliveira, D., Azibeiro, L. A., Marino, M., Maiorano, P., Cortina, A., Cacho, I., and Grimalt, J. O.: A new perspective of the Alboran Upwelling System reconstruction during the Marine Isotope Stage 11: A high-resolution coccolithophore record, Quat. Sci. Rev., 245, 106520, https://doi.org/10.1016/j.quascirev.2020.106520, 2020.

Graly, J. A. and Rezvanbehbahani, S.: Geological and glacial-hydrologic controls on chemical weathering in the subglacial environment, Ann. Glaciol., 63, 165–170, https://doi.org/10.1017/aog.2023.56, 2022.

Graly, J. A., Humphrey, N. F., and Licht, K. J.: Two Metrics Describing the Causes of Seasonal and Spatial Changes in Subglacial Aqueous Chemistry, Front. Earth Sci. (Lausanne)., 6, https://doi.org/10.3389/feart.2018.00195, 2018.

Habicht, K. S. and Canfield, D. E.: Isotope fractionation by sulfate-reducing natural populations and the isotopic composition of sulfide in marine sediments, Geology, 29, 555, https://doi.org/10.1130/0091-7613(2001)029<0555:IFBSRN>2.0.CO;2, 2001.

Haeberli, W., Hoelzle, M., Paul, F., and Zemp, M.: Integrated monitoring of mountain glaciers as key indicators of global climate change: the European Alps, Ann. Glaciol., 46, 150–160, https://doi.org/10.3189/172756407782871512, 2007.

Hawkings, Jon. R., Bradley, J. A., Doting, E. L., Hassan, N., Hendry, K. R., Holt, A. D., Hood, E., Spencer, R. G. M., Stibal, M., Tranter, M., Venturelli, R. A., Wadham, J. L., and Bhatia, M. P.: Glacier biogeochemical cycling and downstream impacts, Nat. Rev. Earth Environ., 7, 124–143, https://doi.org/10.1038/s43017-025-00751-1, 2025.

https://doi.org/10.5194/egusphere-2026-2840
Preprint. Discussion started: 16 June 2026


Hodson, A., Nowak, A., and Christiansen, H.: Glacial and periglacial floodplain sediments regulate hydrologic transfer of reactive iron to a high arctic fjord, Hydrol. Process., 30, 1219–1229, https://doi.org/10.1002/hyp.10701, 2016.

Honiat, A., Baker, J. L., Moseley, G. E., Trüssel, M., Edwards, R. L., and Spötl, C.: Climate sensitivity and glacial inception in the European Alps across marine isotope stage 11 and 10, Quat. Sci. Rev., 384, 110003, https://doi.org/10.1016/j.quascirev.2026.110003, 2026.

Hu, H.-M., Marino, G., Pérez-Mejías, C., Spötl, C., Yokoyama, Y., Yu, J., Rohling, E., Kano, A., Ludwig, P., Pinto, J. G., Michel, V., Valensi, P., Zhang, X., Jiang, X., Mii, H.-S., Chien, W.-Y., Tsai, H.-C., Sung, W.-H., Hsu, C.-H., Starnini, E., Zunino, M., and Shen, C.-C.: Sustained North Atlantic warming drove anomalously intense MIS 11c interglacial, Nat. Commun., 15, 5933, https://doi.org/10.1038/s41467-024-50207-1, 2024.

Hubbard, B. and Nienow, P.: Alpine subglacial hydrology, Quat. Sci. Rev., 16, 939–955, https://doi.org/10.1016/S0277-3791(97)00031-0, 1997.

Ilyashuk, B. and Ilyashuk, E.: Water–Rock Interaction and Freeze–Thaw Cycles as Drivers of Acid Rock Drainage Generation by a Rock Glacier in the European Alps, ACS ES&T Water, 4, 5264–5274, https://doi.org/10.1021/acsestwater.4c00263, 2024.

Ivy-Ochs, S., Monegato, G., and Reitner, J. M.: The Alps: glacial landforms from the Last Glacial Maximum, in: European Glacial Landscapes, Elsevier, 449–460, https://doi.org/10.1016/B978-0-12-823498-3.00030-3, 2022a.

Ivy-Ochs, S., Monegato, G., and Reitner, J. M.: The Alps: glacial landforms prior to the Last Glacial Maximum, in: European Glacial Landscapes, Elsevier, 283–294, https://doi.org/10.1016/B978-0-12-823498-3.00008-X, 2022b.

Jebasinski, L., Winckler, G., Lamy, F., von Stebut, L., Frick, D. A., Basak, C., Kapuge, A. K. I. U., Farmer, J. R., and Gottschalk, J.: Stepwise Glacial Inception and Prolonged Southern Ocean $CO_2$ Outgassing Linked With Marine Isotope Stage 11, Paleoceanogr. Paleoclimatol., 41, https://doi.org/10.1029/2025PA005307, 2026.

Jouvet, G., Cohen, D., Russo, E., Buzan, J., Raible, C. C., Haeberli, W., Kamleitner, S., Ivy-Ochs, S., Imhof, M. A., Becker, J. K., Landgraf, A., and Fischer, U. H.: Coupled climate-glacier modelling of the last glaciation in the Alps, Journal of Glaciology, 69, 1956–1970, https://doi.org/10.1017/jog.2023.74, 2023.

Kotlarski, S., Gobiet, A., Morin, S., Olefs, M., Rajczak, J., and Samacoïts, R.: 21st Century alpine climate change, Clim. Dyn., 60, 65–86, https://doi.org/10.1007/s00382-022-06303-3, 2023.

https://doi.org/10.5194/egusphere-2026-2840
Preprint. Discussion started: 16 June 2026


Li, H., Spötl, C., and Cheng, H.: A high-resolution speleothem proxy record of the Late Glacial in the European Alps: extending the NALPS19 record until the beginning of the Holocene, J. Quat. Sci., 36, 29–39, https://doi.org/10.1002/jqs.3255, 2021.

Liu, J., Chen, Q., Yang, Y., Wei, H., Laipan, M., Zhu, R., He, H., and Hochella, M. F.: Coupled redox cycling of Fe and Mn in the environment: The complex interplay of solution species with Fe- and Mn-(oxyhydr)oxide crystallization and transformation, Earth. Sci. Rev., 232, 104105, https://doi.org/10.1016/j.earscirev.2022.104105, 2022.

Luetscher, M., Boch, R., Sodemann, H., Spötl, C., Cheng, H., Edwards, R. L., Frisia, S., Hof, F., and Müller, W.: North Atlantic storm track changes during the Last Glacial Maximum recorded by Alpine speleothems, Nat. Commun., 6, 6344, https://doi.org/10.1038/ncomms7344, 2015.

Lüthi, D., Le Floch, M., Bereiter, B., Blunier, T., Barnola, J.-M., Siegenthaler, U., Raynaud, D., Jouzel, J., Fischer, H., Kawamura, K., and Stocker, T. F.: High-resolution carbon dioxide concentration record 650,000–800,000 years before present, Nature, 453, 379–382, https://doi.org/10.1038/nature06949, 2008.

McGillen, M. R. and Fairchild, I. J.: An experimental study of incongruent dissolution of $CaCO_3$ under analogue glacial conditions, Journal of Glaciology, 51, 383–390, https://doi.org/10.3189/172756505781829223, 2005.

Milker, Y., Rachmayani, R., Weinkauf, M. F. G., Prange, M., Raitzsch, M., Schulz, M., and Kučera, M.: Global and regional sea surface temperature trends during Marine Isotope Stage 11, Climate of the Past, 9, 2231–2252, https://doi.org/10.5194/cp-9-2231-2013, 2013.

Milker, Y., Rachmayani, R., Weinkauf, M. F. G., Prange, M., Raitzsch, M., Schulz, M., and Kučera, M.: Global Synthesis of Sea-Surface Temperature Trends During Marine Isotope Stage 11, 13–18, https://doi.org/10.1007/978-3-319-00693-2_3, 2015.

Monegato, G., Gianotti, F., Ivy-Ochs, S., Reitner, J. M., Scardia, G., and Akçar, N.: The Early and Middle Pleistocene glaciations in the Alps, Alpine and Mediterranean Quaternary, 36, 1–22, https://doi.org/10.26382/AMQ.2023.07, 2023.

Montross, S. N., Skidmore, M., Tranter, M., Kivimäki, A.-L., and Parkes, R. J.: A microbial driver of chemical weathering in glaciated systems, Geology, 41, 215–218, https://doi.org/10.1130/G33572.1, 2013.

Moseley, G. E., Spötl, C., Brandstätter, S., Erhardt, T., Luetscher, M., and Edwards, R. L.: NALPS19: sub-orbital-scale climate variability recorded in northern Alpine speleothems during the last glacial period, Climate of the Past, 16, 29–50, https://doi.org/10.5194/cp-16-29-2020, 2020.

Neal, A. L., Techkarnjanaruk, S., Dohnalkova, A., McCready, D., Peyton, B. M., and Geesey, G. G.: Iron sulfides and sulfur species produced at hematite surfaces in the presence of sulfate-

https://doi.org/10.5194/egusphere-2026-2840
Preprint. Discussion started: 16 June 2026


reducing bacteria, Geochim. Cosmochim. Acta, 65, 223–235, https://doi.org/10.1016/S0016-7037(00)00537-8, 2001.

Nehrbass-Ahles, C., Shin, J., Schmitt, J., Bereiter, B., Joos, F., Schilt, A., Schmidely, L., Silva, L., Teste, G., Grilli, R., Chappellaz, J., Hodell, D., Fischer, H., and Stocker, T. F.: Abrupt $CO_2$ release to the atmosphere under glacial and early interglacial climate conditions, Science (1979)., 369, 1000–1005, https://doi.org/10.1126/science.aay8178, 2020.

Oliveira, D., Desprat, S., Rodrigues, T., Naughton, F., Hodell, D., Trigo, R., Rufino, M., Lopes, C., Abrantes, F., and Goni, M. F. S.: The complexity of millennial-scale variability in southwestern Europe during MIS 11, Quat. Res., 86, 373–387, https://doi.org/10.1016/j.yqres.2016.09.002, 2016.

Oppo, D. W., McManus, J. F., and Cullen, J. L.: Abrupt Climate Events 500,000 to 340,000 Years Ago: Evidence from Subpolar North Atlantic Sediments, Science (1979)., 279, 1335–1338, https://doi.org/10.1126/science.279.5355.1335, 1998.

Owen, R., Day, C. C., and Henderson, G. M.: CaveCalc: A new model for speleothem chemistry & isotopes, Comput. Geosci., 119, 115–122, https://doi.org/10.1016/j.cageo.2018.06.011, 2018.

Prestrud Anderson, S., Drever, J. I., and Humphrey, N. F.: Chemical weathering in glacial environments, Geology, 25, 399, https://doi.org/10.1130/0091-7613(1997)025<0399:CWIGE>2.3.CO;2, 1997.

Preusser, F.: Towards a chronology of the Late Pleistocene in the northern Alpine Foreland, Boreas, 33, 195–210, https://doi.org/10.1111/j.1502-3885.2004.tb01141.x, 2004.

Preusser, F., Büschelberger, M., Kemna, H. A., Miocic, J., Mueller, D., and May, J.-H.: Exploring possible links between Quaternary aggradation in the Upper Rhine Graben and the glaciation history of northern Switzerland, International Journal of Earth Sciences, 110, 1827–1846, https://doi.org/10.1007/s00531-021-02043-7, 2021.

Reitner, J. M.: The Imprint of Quaternary Processes on the Austrian Landscape, 47–72, https://doi.org/10.1007/978-3-030-92815-5_3, 2022.

Rinklebe, J. and Shaheen, S. M.: Redox chemistry of nickel in soils and sediments: A review, Chemosphere, 179, 265–278, https://doi.org/10.1016/j.chemosphere.2017.02.153, 2017.

Samborska, K., Halas, S., and Bottrell, S. H.: Sources and impact of sulphate on groundwaters of Triassic carbonate aquifers, Upper Silesia, Poland, J. Hydrol. (Amst)., 486, 136–150, https://doi.org/10.1016/j.jhydrol.2013.01.017, 2013.

Schimmelpfennig, I., Schaefer, J. M., Akçar, N., Koffman, T., Ivy-Ochs, S., Schwartz, R., Finkel, R. C., Zimmerman, S., and Schlüchter, C.: A chronology of Holocene and Little Ice Age glacier culminations of the Steingletscher, Central Alps, Switzerland, based on high-sensitivity

https://doi.org/10.5194/egusphere-2026-2840
Preprint. Discussion started: 16 June 2026


beryllium-10 moraine dating, Earth Planet. Sci. Lett., 393, 220–230, https://doi.org/10.1016/j.epsl.2014.02.046, 2014.

Seguinot, J., Ivy-Ochs, S., Jouvet, G., Huss, M., Funk, M., and Preusser, F.: Modelling last glacial cycle ice dynamics in the Alps, Cryosphere, 12, 3265–3285, https://doi.org/10.5194/tc-12-3265-2018, 2018.

Sharp, M., Parkes, J., Cragg, B., Fairchild, I. J., Lamb, H., and Tranter, M.: Widespread bacterial populations at glacier beds and their relationship to rock weathering and carbon cycling, Geology, 27, 107, https://doi.org/10.1130/0091-7613(1999)027<0107:WBPAGB>2.3.CO;2, 1999.

Sinclair, D. J.: Two mathematical models of Mg and Sr partitioning into solution during incongruent calcite dissolution, Chem. Geol., 283, 119–133, https://doi.org/10.1016/j.chemgeo.2010.05.022, 2011.

Singh, S. K., Subramanian, V., and Gibbs, R. J.: Hydrous FE and MN oxides — scavengers of heavy metals in the aquatic environment, Critical Reviews in Environmental Control, 14, 33–90, https://doi.org/10.1080/10643388409381713, 1984.

Skiba, V. and Fohlmeister, J.: Contemporaneously growing speleothems and their value to decipher in-cave processes – A modelling approach, Geochim. Cosmochim. Acta, 348, 381–396, https://doi.org/https://doi.org/10.1016/j.gca.2023.03.016, 2023.

Skiba, V., Spötl, C., Trüssel, M., Schröder-Ritzrau, A., Schröder, B., Frank, N., Eichstädter, R., Tjallingii, R., Marwan, N., Zhang, X., and Fohlmeister, J.: Millennial-scale climate variability in the Northern Hemisphere influenced glacier dynamics in the Alps around 250,000 years ago, Commun. Earth Environ., 4, 426, https://doi.org/10.1038/s43247-023-01083-y, 2023a.

Skiba, V., Jouvet, G., Marwan, N., Spötl, C., and Fohlmeister, J.: Speleothem growth and stable carbon isotopes as proxies of the presence and thermodynamical state of glaciers compared to modelled glacier evolution in the Alps, Quat. Sci. Rev., 322, 108403, https://doi.org/10.1016/j.quascirev.2023.108403, 2023b.

Sommer, C., Malz, P., Seehaus, T. C., Lippl, S., Zemp, M., and Braun, M. H.: Rapid glacier retreat and downwasting throughout the European Alps in the early 21st century, Nat. Commun., 11, 3209, https://doi.org/10.1038/s41467-020-16818-0, 2020.

Spötl, C. and Mangini, A.: Speleothems and paleoglaciers, Earth Planet. Sci. Lett., 254, 323–331, https://doi.org/10.1016/j.epsl.2006.11.041, 2007.

Spötl, C., Mangini, A., and Richards, D. A.: Chronology and paleoenvironment of Marine Isotope Stage 3 from two high-elevation speleothems, Austrian Alps, Quat. Sci. Rev., 25, 1127–1136, https://doi.org/10.1016/j.quascirev.2005.10.006, 2006.

https://doi.org/10.5194/egusphere-2026-2840
Preprint. Discussion started: 16 June 2026


Spötl, C., Scholz, D., and Mangini, A.: A terrestrial U/Th-dated stable isotope record of the Penultimate Interglacial, Earth Planet. Sci. Lett., 276, 283–292, https://doi.org/10.1016/j.epsl.2008.09.029, 2008.

Spötl, C., Baker, J. L., Skiba, V., Honiat, A., Fohlmeister, J., Luetscher, M., and Trüssel, M.: Speleothems in subglacial caves: An emerging archive of glacial climate history and mountain glacier dynamics, Quat. Sci. Rev., 333, 108684, https://doi.org/10.1016/j.quascirev.2024.108684, 2024.

Spratt, R. M. and Lisiecki, L. E.: A Late Pleistocene sea level stack, Climate of the Past, 12, 1079–1092, https://doi.org/10.5194/cp-12-1079-2016, 2016.

Stachnik, Ł., Majchrowska, E., Yde, J. C., Nawrot, A. P., Cichała-Kamrowska, K., Ignatiuk, D., and Piechota, A.: Chemical denudation and the role of sulfide oxidation at Werenskioldbreen, Svalbard, J. Hydrol. (Amst)., 538, 177–193, https://doi.org/10.1016/j.jhydrol.2016.03.059, 2016.

Sun, J., Kobayashi, T., Strosnider, W. H. J., and Wu, P.: Stable sulfur and oxygen isotopes as geochemical tracers of sulfate in karst waters, J. Hydrol. (Amst)., 551, 245–252, https://doi.org/10.1016/j.jhydrol.2017.06.006, 2017.

Szynkiewicz, A., Talon Newton, B., Timmons, S. S., and Borrok, D. M.: The sources and budget for dissolved sulfate in a fractured carbonate aquifer, southern Sacramento Mountains, New Mexico, USA, Applied Geochemistry, 27, 1451–1462, https://doi.org/10.1016/j.apgeochem.2012.04.011, 2012.

Taylor, B. E. and Wheeler, M. C.: Sulfur- and Oxygen-Isotope Geochemistry of Acid Mine Drainage in the Western United States, 481–514, https://doi.org/10.1021/bk-1994-0550.ch030, 1993.

Timmermann, A., Yun, K. S., Raia, P., Ruan, J., Mondanaro, A., Zeller, E., Zollikofer, C., Ponce de León, M., Lemmon, D., Willeit, M., and Ganopolski, A.: Climate effects on archaic human habitats and species successions, Nature, 604, 495–501, https://doi.org/10.1038/s41586-022-04600-9, 2022.

Torres, M. A., Moosdorf, N., Hartmann, J., Adkins, J. F., and West, A. J.: Glacial weathering, sulfide oxidation, and global carbon cycle feedbacks, Proceedings of the National Academy of Sciences, 114, 8716–8721, https://doi.org/10.1073/pnas.1702953114, 2017.

Tzedakis, P. C.: The MIS 11 – MIS 1 analogy, southern European vegetation, atmospheric methane and the "early anthropogenic hypothesis," Climate of the Past, 6, 131–144, https://doi.org/10.5194/cp-6-131-2010, 2010.

Tzedakis, P. C., Hodell, D. A., Nehrbass-Ahles, C., Mitsui, T., and Wolff, E. W.: Marine Isotope Stage 11c: An unusual interglacial, Quat. Sci. Rev., 284, 107493, https://doi.org/10.1016/j.quascirev.2022.107493, 2022.

https://doi.org/10.5194/egusphere-2026-2840
Preprint. Discussion started: 16 June 2026


Vázquez Riveiros, N., Waelbroeck, C., Skinner, L., Duplessy, J.-C., McManus, J. F., Kandiano, E. S., and Bauch, H. A.: The "MIS 11 paradox" and ocean circulation: Role of millennial scale events, Earth Planet. Sci. Lett., 371–372, 258–268, https://doi.org/10.1016/j.epsl.2013.03.036, 2013.

Vera-Polo, P., Sadori, L., Jiménez-Moreno, G., Masi, A., Giaccio, B., Zanchetta, G., Tzedakis, P. C., and Wagner, B.: Climate, vegetation, and environmental change during the MIS 12-MIS 11 glacial-interglacial transition inferred from a high-resolution pollen record from the Fucino Basin of central Italy, Palaeogeogr. Palaeoclimatol. Palaeoecol., 655, 112486, https://doi.org/10.1016/j.palaeo.2024.112486, 2024.

Wadham, J. L., Cooper, R. J., Tranter, M., and Bottrell, S.: Evidence for widespread anoxia in the proglacial zone of an Arctic glacier, Chem. Geol., 243, 1–15, https://doi.org/10.1016/j.chemgeo.2007.04.010, 2007.

Wadham, J. L., Tranter, M., Skidmore, M., Hodson, A. J., Priscu, J., Lyons, W. B., Sharp, M., Wynn, P., and Jackson, M.: Biogeochemical weathering under ice: Size matters, Global Biogeochem. Cycles, 24, https://doi.org/10.1029/2009GB003688, 2010.

Wassenburg, J. A., Samanta, A., Sha, L., Lee, H., Scholz, D., Cheng, H., Stoll, B., Ait Brahim, Y., Budsky, A., and Breitenbach, S. F. M.: Trace element partitioning controls on cave drip water compositions through prior calcite and aragonite precipitation, Commun. Earth Environ., 5, 488, https://doi.org/10.1038/s43247-024-01648-5, 2024.

Weissert, H. and Mohr, H.: Late Jurassic climate and its impact on carbon cycling, Palaeogeogr. Palaeoclimatol. Palaeoecol., 122, 27–43, https://doi.org/10.1016/0031-0182(95)00088-7, 1996.

Wilcox, P. S., Honiat, C., Trüssel, M., Edwards, R. L., and Spötl, C.: Exceptional warmth and climate instability occurred in the European Alps during the Last Interglacial period, Commun. Earth Environ., 1, 57, https://doi.org/10.1038/s43247-020-00063-w, 2020.

Williams, M. W., Knauf, M., Caine, N., Liu, F., and Verplanck, P. L.: Geochemistry and source waters of rock glacier outflow, Colorado Front Range, Permafr. Periglac. Process., 17, 13–33, https://doi.org/10.1002/ppp.535, 2006.

Wynn, P. M., Hodson, A., and Heaton, T.: Chemical and Isotopic Switching within the Subglacial Environment of a High Arctic Glacier, Biogeochemistry, 78, 173–193, https://doi.org/10.1007/s10533-005-3832-0, 2006.

Wynn, P. M., Fairchild, I. J., Baker, A., Baldini, J. U. L., and McDermott, F.: Isotopic archives of sulphate in speleothems, Geochim. Cosmochim. Acta, 72, 2465–2477, https://doi.org/10.1016/j.gca.2008.03.002, 2008.

https://doi.org/10.5194/egusphere-2026-2840
Preprint. Discussion started: 16 June 2026


Wynn, P. M., Morrell, D. J., Tuffen, H., Barker, P., Tweed, F. S., and Burns, R.: Seasonal release of anoxic geothermal meltwater from the Katla volcanic system at Sólheimajökull, Iceland, Chem. Geol., 396, 228–238, https://doi.org/10.1016/j.chemgeo.2014.12.026, 2015.

Wynn, P. M., Fairchild, I. J., Borsato, A., Spötl, C., Hartland, A., Baker, A., Frisia, S., and Baldini, J. U. L.: Sulphate partitioning into calcite: Experimental verification of pH control and application to seasonality in speleothems, Geochim. Cosmochim. Acta, 226, 69–83, https://doi.org/10.1016/j.gca.2018.01.020, 2018.

Yun, K.-S., Timmermann, A., Lee, S.-S., Willeit, M., Ganopolski, A., and Jadhav, J.: A transient coupled general circulation model (CGCM) simulation of the past 3 million years, Climate of the Past, 19, 1951–1974, https://doi.org/10.5194/cp-19-1951-2023, 2023.

Zarroca, M., Roqué, C., Linares, R., Salminci, J. G., and Gutiérrez, F.: Natural acid rock drainage in alpine catchments: A side effect of climate warming, Science of The Total Environment, 778, 146070, https://doi.org/10.1016/j.scitotenv.2021.146070, 2021.

Zekollari, H., Schuster, L., Maussion, F., Hock, R., Marzeion, B., Rounce, D. R., Compagno, L., Fujita, K., Huss, M., James, M., Kraaijenbrink, P. D. A., Lipscomb, W. H., Minallah, S., Oberrauch, M., Van Tricht, L., Champollion, N., Edwards, T., Farinotti, D., Immerzeel, W., Leguy, G., and Sakai, A.: Glacier preservation doubled by limiting warming to 1.5°C versus 2.7°C, Science (1979)., 388, 979–983, https://doi.org/10.1126/science.adu4675, 2025.

Zemp, M., Jakob, L., Dussaillant, I., Nussbaumer, S. U., Gourmelen, N., Dubber, S., A, G., Abdullahi, S., Andreassen, L. M., Berthier, E., Bhattacharya, A., Blazquez, A., Boehm Vock, L. F., Bolch, T., Box, J., Braun, M. H., Brun, F., Cicero, E., Colgan, W., Eckert, N., Farinotti, D., Florentine, C., Floricioiu, D., Gardner, A., Harig, C., Hassan, J., Hugonnet, R., Huss, M., Jóhannesson, T., Liang, C.-C. A., Ke, C.-Q., Khan, S. A., King, O., Kneib, M., Krieger, L., Maussion, F., Mattea, E., McNabb, R., Menounos, B., Miles, E., Moholdt, G., Nilsson, J., Pálsson, F., Pfeffer, J., Piermattei, L., Plummer, S., Richter, A., Sasgen, I., Schuster, L., Seehaus, T., Shen, X., Sommer, C., Sutterley, T., Treichler, D., Velicogna, I., Wouters, B., Zekollari, H., and Zheng, W.: Community estimate of global glacier mass changes from 2000 to 2023, Nature, 639, 382–388, https://doi.org/10.1038/s41586-024-08545-z, 2025.